Contributions to Mineralogy and Petrology (2022) 177:9
https://doi.org/10.1007/s00410-021-01853-x

ORIGINAL PAPER

Crustal storage and ascent history of the Mt. Shasta primitive magnesian andesite: implications for arc magma crustal flux rates

Mitchell Phillips[1,2] · **C. B. Till**[1]

Received: 11 August 2020 / Accepted: 12 October 2021

Abstract

Primitive arc magmas provide our closest glimpse of the original mantle-derived magmas that produce the more ubiquitous andesites and dacites found in subduction zones and that ultimately construct Earth's continental crust. This study examines the crustal storage and ascent history of the Mt. Shasta primitive magnesian andesite (PMA), a demonstrated parent magma for the voluminous mixed andesites erupted at Mt. Shasta. Our petrographic and geochemical observations of the PMA identify a mid-crustal magma mixing event recorded in multiple populations of reversely zoned clinopyroxene and orthopyroxene phenocrysts. Thermobarometric calculations conducted as part of this study and prior phase equilibrium experiments (Grove et al., Contrib Miner Petrol 145:515–533, 2003; Krawczynski et al., Contrib Miner Petrol 164:317–339, 2012) suggest the PMA experienced storage, mixing, and subsequent crystallization at ~ 500 MPa and ~ 975 °C. Modeling of Fe–Mg interdiffusion between the rims and cores of the reversely zoned pyroxenes suggests this mixing event and the resulting crystal rim growth occurred less than 10 years prior to eruption ($2.9^{+6.4}_{-2.2}$). Ascent from 500 MPa (~ 15 km) during the calculated diffusion timescales suggests minimum crustal transit rates of ~ 170 MPa (~ 5 km)/year and cooling rates of ~ 5–7 °C/km, consistent with conductive cooling models. This ascent rate is slower than the handful of previously documented trans-crustal magmatic ascent rates and significantly slower than syn-eruptive decompression rates. If this behavior is representative, ~ the 10% mafic magmas erupted as part of the modern Mt. Shasta edifice fluxed through the crust within decades. Coupled with a review of the U–Th–Ra residence times for Shasta andesites to dacites, we suggest that crustal magma flux and assembly beneath modern Mt. Shasta occurred in discrete pulses that occupy a minority of the 700 k.y. period of edifice construction. The results of this study thus constrain the pre-eruptive history and ascent characteristics of a hydrous primitive arc magmas in the upper crust between their shallowest storage region in the mid-crust and volatile exsolution and provide constraints on crustal magma flux beneath continental arc volcanoes. Should future earthquake swarms indicative of magma movement in the middle to upper crust occur beneath Shasta, the results presented here also provide the first estimates of the possible magma ascent rates and the time intervals that could accompany related magma ascent to eruption at Mt. Shasta.

Keywords Diffusion chronometry · Pyroxene · High-Mg andesite · Mt. Shasta · Cascades

Introduction

In concert with other petrological and geochemical tools that can constrain magmatic processes and pressure–temperature–composition (*P–T–X*) conditions in magma storage regions, elemental, or isotopic diffusion in minerals and/or melts has become widely used within the last 5–10 years to assess the timescales of a variety of magmatic processes, including magma mixing to eruption, differentiation and cooling, and more recently, magma ascent rates. Studies using mineral-hosted melt embayments (e.g., Lloyd et al. 2014; Ferguson et al. 2016; Myers et al. 2018), melt inclusions (e.g., Ruscitto et al. 2010; Myers et al. 2019), and

Communicated by Mark S Ghiorso.

✉ Mitchell Phillips
mphillips2134@gmail.com

[1] School of Earth and Space Exploration, Arizona State University, Tempe, AZ 85281, USA

[2] Present Address: US Geological Survey, Menlo Park, CA, USA

Published online: 23 December 2021

water-in-olivine (e.g., Barth et al. 2019) have determined rapid, syn-eruptive ascent rates (10's of meters per second [m/s] or more) associated with magma motion in the eruptive column driven by bubble nucleation and growth. However, these syn-eruptive rates only reflect magma movement rates during the very last stage of ascent.

Shifting focus to the rates magmas ascend through the crust prior to volatile exsolution and eruption requires different approaches, which only a few studies have attempted to date. U-series isotopic ratios have the potential to assess trans-crustal magma ascent rates as they reflect the residence time of magma in the crust (Hawkesworth et al. 2004); however, they are applicable only to rocks erupted less than a few hundred thousand years ago and it is often difficult to evaluate the depths associated with crustal storage history. McKenzie (2000) assessed disequilibrium activity ratios of (^{210}Pb/^{226}Ra) and (^{228}Ra/^{232}Th) of MORB to determine the timescales of 6–20 years between last chemical equilibrium with the mantle and appearance on the surface, although actual magma movement rates could not be assessed due to the limitations mentioned above. Blatter and Carmichael (1998) concluded that the presence of dense, 1–2 cm hornblende peridotite xenoliths in low density Central Mexican andesites required a minimum ascent rate of ~ 26 km/day based on Stoke's settling velocity. Ruprecht and Plank (2013) utilized measurements of Ni diffusion in olivine to assess mantle melting-to-eruption timescales for primitive magmas feeding Irazu volcano, a large stratocone in the Central American arc, and found integrated trans-crustal magma ascent rates of 10's of m/day (~ 68 m/day). Similarly, recent Fe–Mg, Ni and Mn in olivine diffusion chronometry constrained transit times of ~ 10 days from near-Moho conditions to eruption for primitive magmas erupted in northern Iceland, suggesting ascent rates of 100's of m/day (Mutch et al. 2019). Though these studies conclude various trans-crustal magma ascent rates, these rates are integrated histories from the mantle source to the surface. Therefore, these rates are less likely to reflect a specific rate that magma actually traveled, especially within the upper crust. To date only one other study has determined a diffusion timescale associated with mixing in the low-to-mid-crust to eruption; this study of a basaltic andesite erupted at a cinder cone in the Lassen Volcanic Field implies maximum average upper crustal ascent rates of ~ 2.5 m/day (Hollyday et al. 2020). The relative paucity of such estimates leaves many questions as to how characteristic these rates are, as well the relative importance of the primary magma compositions, volatile content, tectonic setting, and eruption initiation mechanism, in dictating these rates. This study utilizes primitive hydrous magma erupted in from a satellite vent at Mt. Shasta with well constrained experimental phase equilibria to work toward these questions and more effectively probe the storage history and ascent characteristics recorded in hydrous primitive arc magmas.

Mafic eruption products from satellite cinder cones, as well as quenched, primitive mafic inclusions in arc andesites have informed our understanding of mantle melting in subduction zones, showing that mantle wedge lithologies ± slab melting in the presence of water, reactive porous flow, followed by subsequent crustal fractionation and mixing of H_2O-rich melts with variable addition of lower crustal melts, are dominantly responsible for the voluminous andesitic to dacitic magmas that build arc stratovolcanoes (e.g., Gill 1981; Sisson and Layne 1993; Grove et al. 2005, 2012; Kelemen et al. 2013; Walowski et al. 2015). In this study, we investigate the high-Mg, primitive magnesian andesite (PMA) from Mt. Shasta. Though pyroxene andesites and dacites are the volumetrically dominant product erupted at Mt. Shasta (Grove et al. 2002, 2003, 2005), the PMA has been identified as the near-primary parent magma to the more evolved dacites and andesites in the Mt. Shasta magmatic system (e.g., Grove et al. 2005; Barr et al. 2007; Krawczynski et al. 2012). The PMA erupted after minimal crustal fractionation from a satellite vent ~ 19 km north of the Mt. Shasta summit, effectively by-passing the complex plumbing system and multiple crystallization depths of andesites and dacites erupted in the main edifice. Experiments on the PMA (Grove et al. 2003; Krawczynski et al. 2012) have determined the *P–T* conditions of the phenocryst crystallization, particularly their outermost rim formation, thereby constraining the compositional evolution of the mafic phases and better calibrating the crustal storage conditions experienced by the PMA.

This study utilizes in situ mineral geochemistry, whole rock major and minor element geochemistry, thermobarometric calculations, petrographic investigations, and Fe–Mg exchange diffusion chronometry along with the pre-previously published experimental phase relations to investigate pre-eruptive storage history and crustal ascent rates of the PMA magma. Unlike previous assessments of magma ascent rates from an ambiguous depth in the mantle or those reflective of syn-eruptive rates in the conduit, this study identifies a magmatic process associated with a specific depth in the crust and determines the likely subsequent magma ascent rates through the upper crustal. Results of this study will inform our knowledge of the petrogenesis and ascent timescales of the PMA and its role as a hydrous near-primary parent magma of more evolved Mt. Shasta andesites and dacites. In addition, establishing ascent timescales through this method improves volcanic hazard models for cinder cones and similar magma types in the southern Cascades and provides the grounds for further studies to investigate other arc volcanic systems.

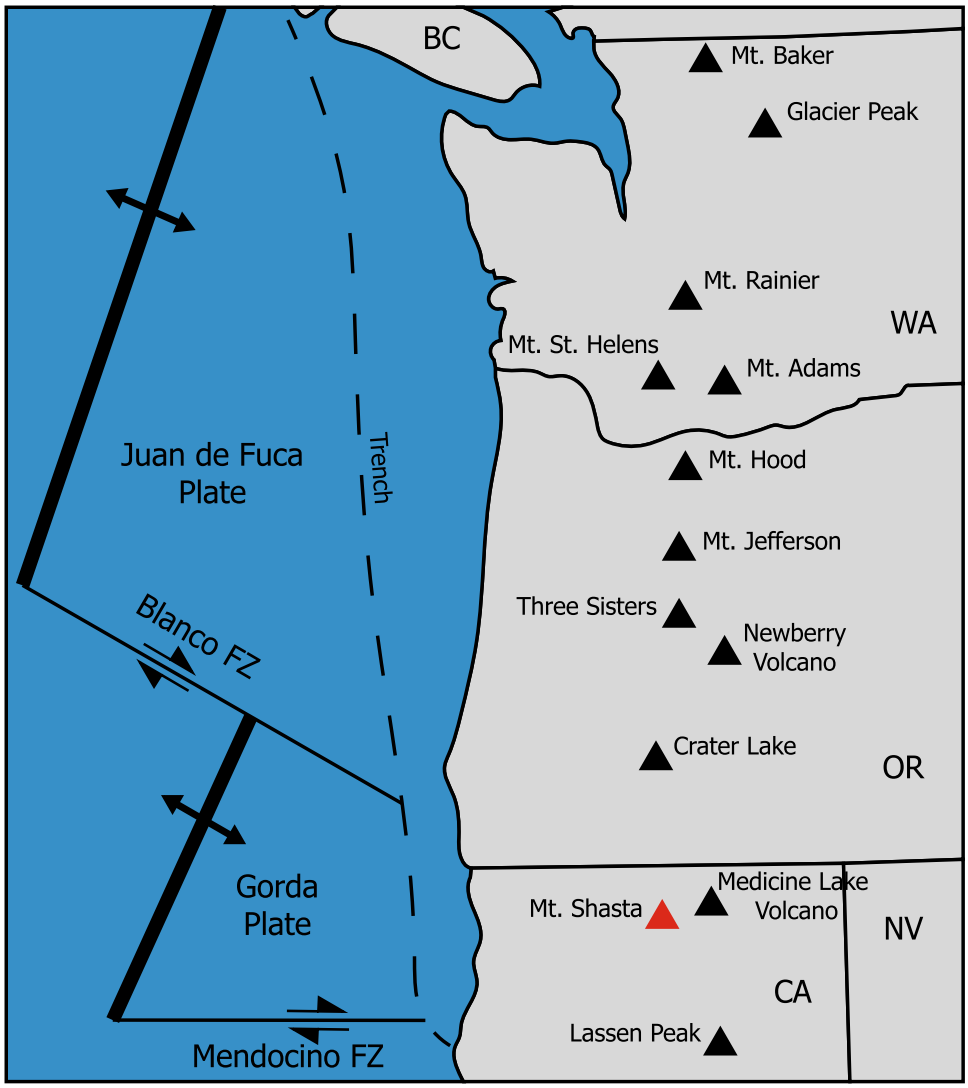

Fig. 1 Map to provide regional context for Mt. Shasta in the greater Cascades range. Each Cascades volcano is signified by a black triangle, with Mt. Shasta in red

Geologic setting and prior work

Mt. Shasta, or Úytaahkoo as it was originally named, is an andesitic stratocone volcano, located in the southern reach of the Cascades, or Yamakiasham Yaina, volcanic chain, ~ 130 km (km) northwest of the Lassen Volcanic field and 60 km west of the Medicine Lake, a large rear-arc volcano (Fig. 1). Tectonic and volcanic activity in the Mt. Shasta region is the product of northwestern subduction of the young ~ 12–14 Mya Gorda Plate beneath the North American plate at ~ 4 cm/year (Green and Harry 1999; Demets et al. 2010). The young age of the underlying plate results in the Cascades being one of, if not the, warmest subduction zone on Earth today (e.g., Syracuse et al. 2010). These relatively warm thermal parameters and the resulting depths of subducting lithosphere dehydration (e.g.,Syracuse et al. 2010; van Keken et al. 2011), the location near the southern edge of the Cascades subduction zone (e.g., Till et al. 2013), and potentially the location of the subducting Blanco fracture zone (Embley and Wilson 1992), all may influence why Mt. Shasta is one of the most productive and hazardous volcanoes in the Cascades today (e.g., Ewert et al. 2018; Mangan et al. 2019; Till et al. 2019; Christiansen et al. 2020). Tertiary sandstones, shales, and andesitic volcanics, Mesozoic granites, ultramafics of the Trinity ophiolite, and Paleozoic metasedimentary rocks all uncomformably underlie the Mt. Shasta edifice (Griscom 1980; Blakely et al. 1985; Fuis et al. 1987). Mt. Shasta is thought to have had four major eruptive episodes over the last ~ 250,000 years (Christiansen et al. 1977): Sargents Ridge [~ 25,000 to ~ 130,000 years before present (ybp)], Misery Hill (~ 80,000–10,000 ybp), Shastina (~ 10,000–9400 ybp), and Hotlum (~ 6000–2000 ybp) which forms the modern summit (14,162 ft.). The Mt. Shasta stratocone is primarily composed of andesite and dacite flows, dacite domes, and pyroclastic flow deposits fed by an H_2O-rich parental magma, as exemplified by the primitive magnesian andesite (PMA) (Grove et al. 2003).

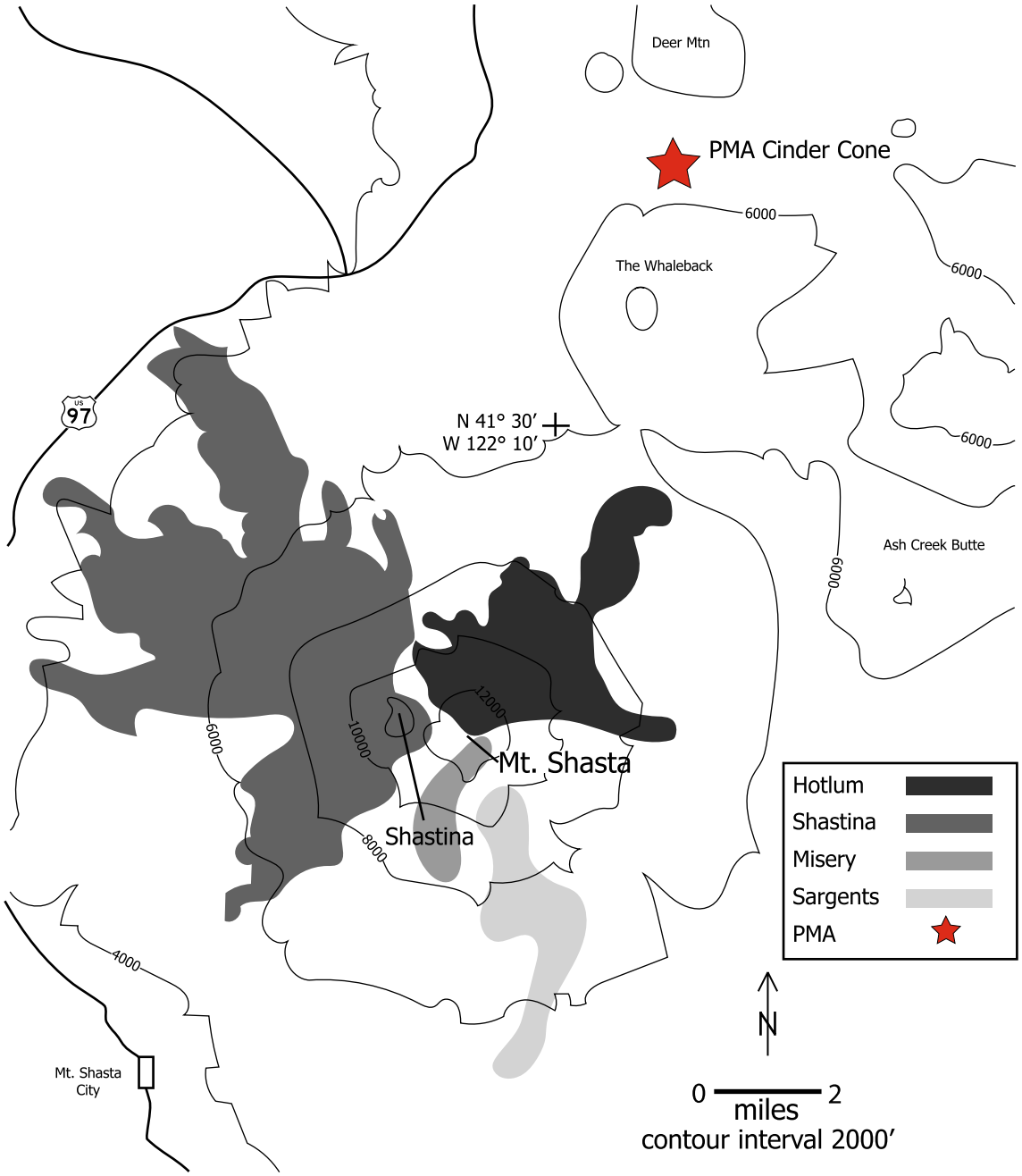

Fig. 2 Map of the Mt. Shasta area showing approximate locations of Quaternary cone building eruptive periods (Baker et al. 1994; Grove et al. 2002). This map shows the four major eruptive episodes over the last ~ 250,000 years (Christiansen et al. 1977): Sargents Ridge [~ 250,00 to ~ 130,000 years before present (ybp)], Misery Hill (~ 80,000–10,000 ybp), Shastina (~ 10,000–9400 ybp), and Hotlum (~ 6000–2000 ybp) which forms the modern summit (14,162 ft.). The primitive magnesian andesite (PMA) is highlighted as a red star

The PMA of Mt. Shasta is exposed at a cinder cone ~ 19 km north–northeast of the Mt. Shasta summit, in the saddle between Deer Mountain and The Whaleback (Fig. 2). Recent work indicates that the PMA cinder cone and related lava to the west in the Deer Mountain/Whaleback area, totaling ~ 0.03–0.05 km^3, were likely erupted ~ 700 ka, coeval with early construction of the present-day Mt. Shasta edifice 18 km southwest (A. Calvert, written communication, 2021). The cinder cone edifice is densely vegetated and quarried, providing a cross-sectional view of the interior structure and access to the earliest erupted materials. Strong stratifications of red to gray cinders and bombs indicate short lived, oscillatory eruptions, which are common at cinder cones (Pioli et al.

2009). Indurated blocks and bombs consist of porphyritic olivine–augite lava with a dark gray, aphanitic groundmass.

Prior studies conducted phase equilibrium experiments on the PMA over conditions of 0.1–800 MPa and 940–1250 °C (Grove et al. 2003; Krawczynski et al. 2012). Experimental results of Grove et al. (2003) confirmed the PMA's role as the near-primary hydrous precursor of voluminous Mt. Shasta dacites and andesites, and concluded the PMA crystallized at or near water-saturated conditions with pre-eruptive H_2O contents of > 4.5–6 wt% H_2O, with some lavas having as much as 10 wt% H_2O. Later melt inclusion work on the PMA by Ruscitto et al. (2011) confirmed these H_2O contents. Experiments from Krawczynski et al. (2012) interrogated the stability of pyroxene, olivine, plagioclase, and amphibole in the PMA. Several of the Krawczynski et al. (2012) experiments, specifically experiments 41–107b and 41–119b (Table 1), were H_2O-saturated and performed at nearly identical *P–T* conditions but different fO_2 conditions (NNO and NNO + 3, respectively). 41–107b, conducted at nickel–nickel oxide buffer (NNO), produced a phase assemblage that more closely resembles that observed in the PMA natural samples, including lacking amphibole, compared to 41–119b (conducted at NNO + 3), which contains amphibole. Thus, both Krawczynski et al. (2012), and earlier related experiments of Grove et al. (2005), suggest the phase assemblage and phenocryst compositions observed in the PMA are produced at oxygen fugacities (fO_2) approximated by the NNO buffer.

The results of these experiments are central to how the PMA is now understood, though other studies have attempted to explain the crystal assemblage of the PMA through different means. Streck et al. (2007) and Streck and Leeman (2018) argues that PMA was not the result of extensive hydrous mantle melting, as described by Grove et al. (2002), but rather as a result of magma mixing and crustal contamination. They cite the mixing of other Shasta region lavas, predominantly between the Shastina dacite and the high-alumina olivine tholeiite (HAOT) (Grove et al. 2005), as the origin of the PMA pyroxene compositions and crustal contamination from the underlying Trinity ophiolite (Quick 1981) as the origin of the PMA olivine "xenocrysts". Streck et al. (2007) and Streck and Leeman (2018) also argue that the PMA is not parental to further fractionated andesites and dacites in the Shasta region. In a reply to Streck et al. (2007), Barr et al. (2007) points out that olivine from the Trinity ophiolite differs from those in the PMA, particularly in chromium (Cr) composition and Fo-content, with the PMA olivine being more magnesian. Keleman and Yogodzinski (2007) also replied to Streck et al (2007), discussing the occurrence of a PMA in the Aleutians that was central in the genesis of more fractioned magmas in that system. This paper agrees with Streck et al. (2007) and Streck and Leeman (2018) in that the PMA likely experienced a multi-stage petrogenetic history, but differs by suggesting that the PMA olivine are likely to be the result of extensive hydrous mantle melting as described in Grove et al. (2002, 2003, 2005) and in agreeing with Barr et al. (2007) that the PMA is the likely parental magma of many Shasta region lavas.

The pulsatory nature of short-lived, small volume eruptions at cinder cones provides a concise window into the mixing history and generation of primitive magmas at small mafic arc-related volcanoes. Their relatively un-evolved eruptive products maintain geochemical signatures imparted during genesis and imprinted on the magma during its rapid

Table 1 Experimentally derived clinopyroxene and orthopyroxene compositions from Krawczynski et al. 2012 runs 41–107b and 41–119b compared to average clinopyroxene and orthopyroxene rim compositions

Sample/run	Temperature	Pressure	SiO_2	TiO_2	Al_2O_3	Cr_2O_3	FeO	MnO	MgO	CaO	Na_2O	K_2O
Clinopyroxene												
41–107b	975	490	54	0.29	1.77	0.51	5.5	0.13	17.9	20.13	0.29	0
41–119b	975	500	52.9	0.26	2.15	0.44	4.7	0.11	17.6	20.96	0.31	0
PMA (avg rim)	975*	500*	53.3	0.2	2.0	0.9	4.2	0.1	18.6	20.4	0.2	0.0
Orthopyroxene												
41–107b	975	490	56.3	0.07	1.37	0.31	8.1	0.14	32.8	1.58	0.07	0
41–119b	975	500	56.8	0.1	1.45	0.24	7.4	0.17	32.8	1.23	0.04	0
PMA (avg rim)	975*	500*	56.2	0.1	1.4	0.3	8.8	0.2	31.4	1.8	0.0	0.0

Table 2 Bulk major element geochemistry of Mt. Shasta primitive magnesian andesite via X-ray Fluorescence performed by the Washington State University geoanalytical lab

SiO_2	TiO_2	Al_2O_3	FeO*	MnO	MgO	CaO	Na_2O	K_2O	P2O5	LOI %
57.58	0.58	14.51	5.64	0.1	8.55	8.02	3	0.75	0.12	0.35

ascent. Prior work has studied the timescales associated with rapid ascent and emplacement of deeply extracted magma at larger, more evolved composite stratocones (Ruprecht and Plank 2013), but little work has been done on primitive arc magmas erupted at cinder cones despite their primitive compositions suggesting a straightforward crustal ascent. While the PMA is still the most primitive hydrous magma thought to have erupted in the modern-day Mt. Shasta region (MgO > 8.5 wt%; H_2O > 4.5 wt%; Table 2) (Grove et al. 2005), the presence of a range of cpx and opx compositions with reverse chemical zoning in the crystal cargo do not suggest that it ascended directly from near-Moho depths to eruption. Rather, the crystal cargo suggests that the PMA experienced a multi-stage history of minimal fractionation and magma mixing in the mid-crust prior to eruption, the details of which are the focus of this study.

Methods and samples

Samples

Eight near-vent poorly vesiculated spatter samples were collected from the PMA cinder cone for this study. Petrographic investigations on 27 resulting thin sections established their phenocryst and groundmass assemblages, grain size and abundance, and textural relationships. Fresh cutoffs from thin section preparation were sent for major and trace element geochemistry via X-ray Fluorescence (XRF) and Inductively Coupled Plasma Mass Spectrometry (ICP-MS) at the Washington State University GeoAnalytical lab.

Phenocryst major element compositions

Eight polished sections with high pyroxene abundances were carbon coated and imaged with backscatter electron (BSE) images, as well as analyzed for compositional transects of major elements across the outer zone boundary via wave-dispersive spectroscopy, using the JXA-8530F Electron Probe Micro-analyzer in the Eyring Materials Center at Arizona State University. EPMA compositional transects were collected at 20 kV and 20 nA using a 1 µm beam diameter and 5 µm step size to mitigate convolution. All the BSE images used for diffusion modeling were collected at an accelerating voltage of 20 kV. Diffusion anisotropy and c-axis growth effects (Allan and Mavko 2013; Krimer and Costa 2017) were mitigated by measuring transects orthogonally to the (100) crystallographic plane and parallel to the (010) crystallographic plane. Crystallographic orientations were determined by crystal shape, cleavage, and interference colors. One EPMA transect of major element compositions from Mg-rich rims to Fe-rich cores was measured on each of the 21 representative clinopyroxene and 13 representative orthopyroxene phenocrysts. Hornblende, hypersthene, and augite standards were analyzed at the beginning and end of each analytical session to ensure accurately reproduced compositions from the detectors. High-resolution BSE images were taken during analytical sessions for grayscale profile measurements.

BSE image grayscale profiles

Grayscale values of BSE images are a good proxy for Mg# (Mg/(Mg + Fe)) in mafic phenocrysts, such as pyroxenes, with negligible Ca variation (Petrone et al. 2016). Ca diffusion is slower than Fe–Mg interdiffusion (Cherniak and Dimanov 2010) in pyroxene and minimal compositional variation in Ca in these pyroxenes suggest it does not affect the brightness of the BSE image when taken with an accelerating voltage of 20 kV. The equivalency of the BSE contrast and Mg# is corroborated by the Mg# profiles measured in the PMA pyroxene via EPMA to the relative grayscale values extracted for the same transect from BSE images (Fig. 3). Though accelerating voltage affects the absolute grayscale values, our analyses suggest the relative difference in grayscale value between darker, Mg-rich areas and lighter, Fe-rich areas does not appear to change. This equivalency allows for extrapolation of grayscale profiles as a proxy for Fe–Mg exchange without having to directly calibrate the gray values of each image to Mg#, a method also adopted in several recent studies (e.g., Allan and Mavko 2013; Petrone et al. 2016; Conway et al. 2020). Modeling grayscale profiles has the added benefit of providing much higher spatial resolution when compared to modeling Mg# profiles from EPMA transects (~ 0.5 µm pixel resolution of BSE image vs. ~ 5 µm EPMA spot analysis spacing to avoid activation volume convolution) (Fig. 3).

The image processing software ImageJ was used to capture and export grayscale profiles to.csv files from the BSE images (e.g., Allan et al. 2013; Petrone et al. 2016; Krimer and Costa 2017). Specifically, ImageJ was used to capture the greyscale value of pixels in a designated rectangular area (here ~ 5 µm wide by ~ 10 µm long on average), which averages the ~ 20–35 grayscale pixel values across the width of the rectangle into a single linear profile of the specified length, to minimize any small image or crystal heterogeneities. The profiles captured included compositional plateaus on either side of the diffusion profiles and the profiles themselves according to best practices (Krimer and Costa 2017). The lengths of the diffusion portion of the profiles were consistent between pyroxene grains, with most falling within 3.5–5.5 µm, though three profiles were 8–10 µm.

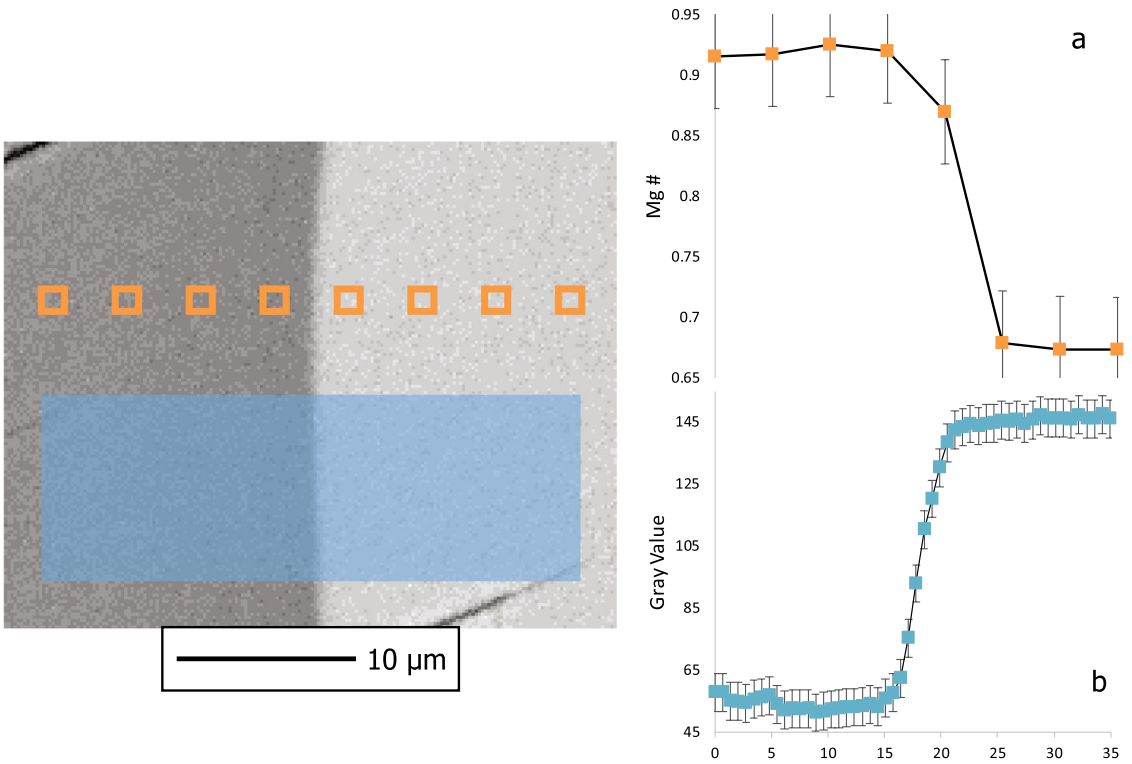

Fig. 3 **a** EPMA compositional profile of Mg# with 5 µm spacing used to justify the grayscale profile **b** along the orthopyroxene zone boundary. Error bars were calculated as the standard error of the mean. BSE grayscale values are used as a proxy for Mg# in clinopyroxene and orthopyroxene with negligible Ca and Al variation across the compositional boundary. Grayscale profiles were used for diffusion modeling as the better spatial resolution produces model profiles with minimal root mean squared misfit

Pressure–temperature–H_2O–fO_2 constraints

Temperature and pressure are inherently coupled with determining timescales and ascent rates of the PMA. Without constraints to provide a reliable thermal history, diffusion modeling will not produce meaningful timescales or ascent rates for the PMA. Given the range of prior phase equilibria experiments (see Sect. 2), these were used, along with secondary checks by mineral thermometry and barometry to identify the temperature and pressure of crystallization the mineral phases in question and construct a conceptual model of the volcanic plumbing system. Specifically, the two-pyroxene thermobarometer of Putirka (2008) was used to confirm the *P*–*T* constraints interpreted from the phase equilibria experiments. The Putirka (2008) thermobarometer assumes chemical equilibrium between cpx/opx pairs, where $K_D(\mathrm{Fe-Mg})^{\mathrm{cpx-opx}} = 1.09 \pm 0.14$ (Putirka 2008). The equations used for these calculations are specifically designed for pyroxenes with Mg# > 0.75. Despite the presence of melt inclusions in some zoned pyroxene phenocryst cores, which have applications outside the scope of this study, no glassy groundmass melt inclusions were found, which precluded the use of mineral–liquid thermobarometry.

Diffusion modeling

All diffusion modeling was conducted using a Monte Carlo approach to solve the analytical solution to the diffusion equation executed in Python (see additional details in Brugman 2020). This approach facilitated exploring a range for each of the input variables as detailed below to determine the temperature–timescale pair that returned the lowest misfit between the modeled and observed concentration profiles, following the approach utilized in Till et al. (2015) and Shamloo and Till (2019). The model was run ten times each for all cpx and opx diffusion profiles, with 20,000 variable values tested each run. 21 profiles were modeled for cpx from 8 thin sections and 13 profiles were modeled for opx from 7 thin sections.

Only measured profiles with at least four data points within the concentration gradient were used for the diffusion modeling to avoid convolution (Costa and Morgan 2011). To determine the diffusion coefficient, the activation energy and pre-exponential diffusion factors of Fe–Mg interdiffusion in cpx and opx from Müller et al. (2013) and Dohmen et al. (2016) were used, respectively. In our models, the appropriate diffusion coefficient was calculated over a

broad temperature range (750–1350 °C) with the following Arrhenius-type equation:

$$D = D_0 \times \exp\left(\frac{-Q - \Delta V\left(P - 10^5\right)}{R \times T}\right),$$

where D is the diffusion coefficient, D_0 is the pre-exponential diffusion factor, Q is the activation energy at 10^5 Pa, ΔV is the activation volume, P is the pressure in Pa, and R is the gas constant. Müller et al. (2013) describes $D_{Fe–Mg}$ to be insensitive to fO_2 over the range of values applicable to the PMA. To date there has not been a study to constrain the effect of H_2O in the pyroxene lattice on $D_{Fe–Mg;}$ however, based on results for olivine, it is likely it would only enhance the diffusion rate and provide shorter timescales then those determined here. The broad range of temperatures allowed for a best fit temperature to be analytically determined using our Monte Carlo approach to further confirm the constraints from thermobarometry and phase equilibria, rather than assuming a single temperature or narrow range of temperature conditions.

The BSE grayscale value profiles were used as a proxy for the Fe–Mg concentration profiles for diffusion chronometry as discussed above. We are only interested in the thermal history recorded in the primary diffusion profile. Consequentially, most of the concentration plateaus on either side of the diffusion profile were not included in diffusion modeling, thereby eliminating their impact on the root mean squared misfit of the modeled profile (Fig. 4). For each profile, a planar source with infinite initial concentrations was assumed. The analytical solution to the following diffusion equation was used to assess timescales:

$$C_{(t,x)} = C_0 + \left(\frac{C_1 - C_0}{2}\right) \times Erfc\left(\frac{x}{2\sqrt{Dt}}\right),$$

where $C_{(t,x)}$ is the composition at point x at time t, C_1 and C_0 are the initial concentrations on each side of the zone boundary, x is the distance from the beginning of the measured profile, D is the diffusivity, and t is the time (Costa and Morgan 2011). The initial concentrations were determined using the maximum and minimum grayscale values of concentration plateaus on either side of the diffusion profile. Plotting the results on probability and cumulative probability functions allows better determination of error associated with timescales derived from this method (Table 3, Figs. 5, 6).

Error reporting

Typically, in modern diffusion chronometry studies a best fit time is found via a Monte Carlo approach for a single temperature or a small range of temperatures, where misfit between modeled and measured profiles is minimized over multiple trials as was done here (e.g., Costa and Morgan

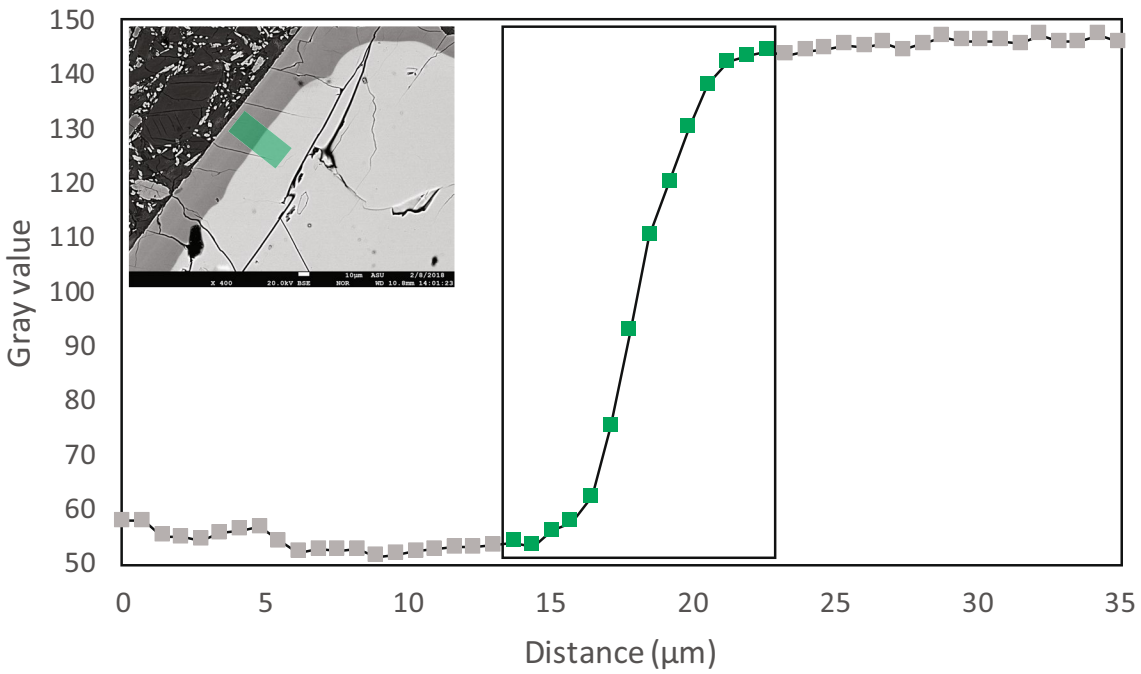

Fig. 4 Example grayscale value profile (dimensionless) vs. distance (μm) used for diffusion modeling. Only the rectangular area with highlighted green squares was used for modeling, greyed out squares are concentration plateaus excluded from modeling to produce minimal root mean square misfit. The inset BSE image shows the area of grayscale values captured for this profile

Table 3 Best fit times and temperature results of each pyroxene grain used for diffusion modeling via the methods discussed in Sect. 3.5

Sample	Best time (years)	Positive error (years)	Negative error (years)	Best temperature (°C)
Clinopyroxene				
01-cpx1	2.93	5.85	1.91	907
01-cpx2	2.93	4.84	1.35	897
01-cpx3	3.28	4.24	1.71	884
04-cpx1	3.12	4.09	1.46	923
04-cpx4	2.75	5.51	1.34	930
04-cpx5	2.69	5.7	1.41	944
04-cpx6	1.57	6.57	0.81	940
08-cpx1	3.26	5.34	1.86	938
08-cpx2	3.43	4.47	1.57	974
08-cpx3	2.78	4.5	1.17	993
11-cpx1	2.25	5.8	1.09	920
11-cpx2	2.94	5.56	1.59	934
11-cpx3	3.46	5.05	2.36	905
12-cpx2	3.45	5.23	1.95	923
12-cpx4	2.84	4.65	1.39	940
12-cpx7	4.5	4.71	2.74	908
16-cpx1	2.99	5.81	1.88	896
16-cpx2	3.25	4.96	1.66	906
16-cpx3	2.87	5.34	1.7	887
22-cpx1	1.98	4.4	0.87	898
23-cpx1	3.25	5.57	1.97	928
Average	2.98			923
Max positive err	6.57			
Max negative err	2.74			
Orthopyroxene				
01-opx1	2.85	6.44	2.05	937
04-opx1	2.77	5.39	1.43	948
04-opx3	2.59	4.59	1.24	985
04-opx4	3.32	4.56	1.58	911
08-opx2	2.35	5.5	1.38	880
08-opx3	3.1	5.57	1.81	919
11-opx1	3.66	5.54	2.24	921
11-opx2	3.43	5.4	2.08	930
12-opx2	3.05	5.43	1.68	945
16-opx1	2.62	4.96	1.23	967
16-opx2	2.97	4.04	1.24	945
22-opx2	2.55	5.03	1.28	982
22-opx3	2.82	5.66	1.55	948
Average	2.93			940
Max positive err	6.44			
Max negative err	2.24			

2011; Till et al. 2015; Shamloo and Till 2019; Costa et al. 2020). This results in a single best fit time and temperature. In actuality, a range of *T*–*t* combinations can solve the analytical solution to the diffusion equation with relatively low misfit (Figs. 5, 6) and many similar studies do not account for the placement of the best fit time amongst the range of times modeled. Here we plot the misfit, calculated as a sum of the square of the residuals between the measured and modeled concentration profiles, as a function of the temperature and time ranges modeled and extract the probability density functions (pdf) for best fit temperature–time pair (Figs. 5, 6). This pdf is then used to determine the asymmetric error on the resulting best fit time. The results produce asymmetric timescale error values, because the range of times is bounded by zero, resulting in the best fit time not being the median value of the low misfit timescale range (Fig. 6). Overall, the relative contribution of the temperature constraints to the overall uncertainty in the timescale calculations is much greater than the uncertainty in the E and D_0 terms in the diffusion coefficient, which is greater than the analytical uncertainty.

Results

PMA lava geochemistry and petrography

The PMA is a calc-alkaline andesite with a higher Mg# (> 0.72) than any other Mt. Shasta area lava (Grove et al. 2005) (Fig. 7, Table 2). Polished sections from three samples display similar relative abundances of large (~ 5–10 mm), unzoned olivine phenocrysts and smaller (~ 2 mm) reversely zoned clinopyroxene and orthopyroxene phenocrysts. Normally zoned, submillimeter skeletal olivine and unzoned clinopyroxene and glomerocrysts of intergrown clinopyroxene and orthopyroxene are present in lesser abundances. The groundmass is glassy with plagioclase microlites, pyroxenes, and olivine and does not indicate any flow-alignment. Phenocrysts are mostly euhedral and make up ~ 15% of the total volume, with glomerocrysts making up < 5%.

Mineral phase major element geochemistry

21 clinopyroxene and 13 orthopyroxene reversely zoned phenocrysts were analyzed for major element profiles. Though core compositions varied between crystal populations, rim compositions varied minimally across all clinopyroxene and orthopyroxene examined, with MgO and SiO_2 concentrations of 18–19 wt% and 52–53 wt% and 33–34 wt% and 56–57 wt%, respectively (Figs. 3, 8). Olivine phenocrysts are Fo_{90} (Table 4) and do no record the same zoning texture of pyroxene phenocrysts. Groundmass plagioclase is An_{70}.

Crystal populations

Clinopyroxene, orthopyroxene, and olivine phenocrysts are separated into five distinct populations based on major

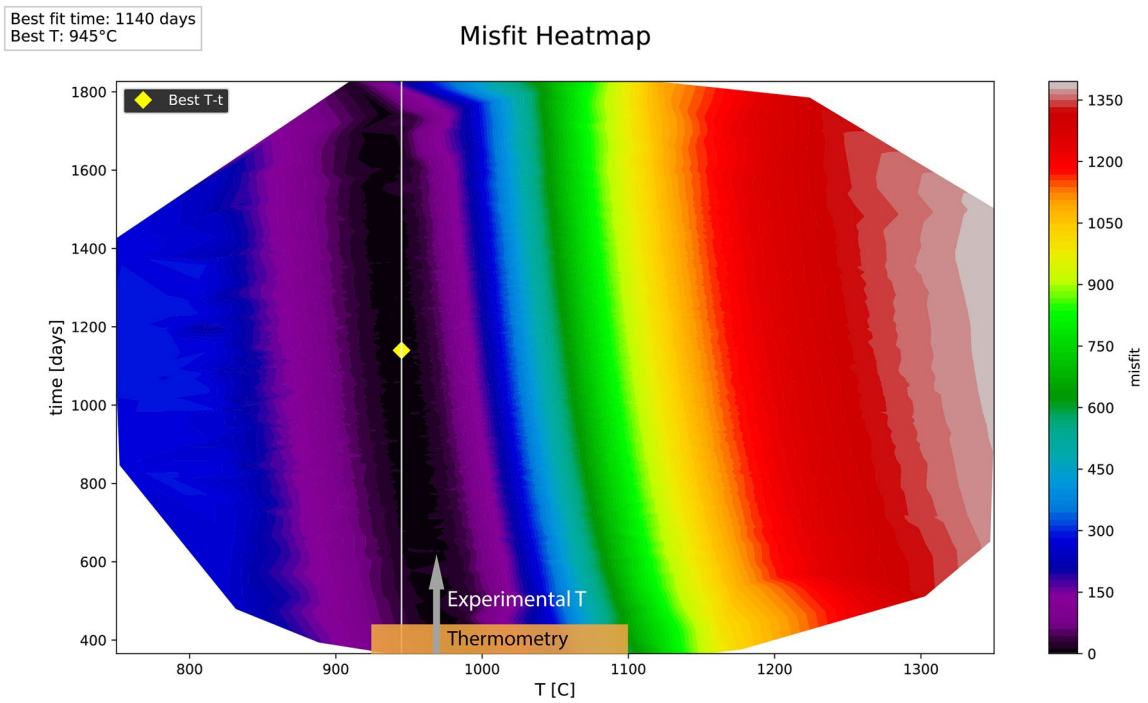

Fig. 5 Misfit heatmap showing the ranges of times and temperatures with associated misfit produced during diffusion modeling with the grayscale value profile of one orthopyroxene phenocryst. Warmer colors are *T–t* values with higher misfit, while cooler colors are *T–t* values with lower misfit. Thermobarometry results (highlighted in orange) and the best experimental *P–T* results match (gray arrow) overlap with the zone of lowest misfit. The yellow diamond represents the best fit time and temperature for this sample, while the white line represents, where the probability distribution function would plot if viewed from above

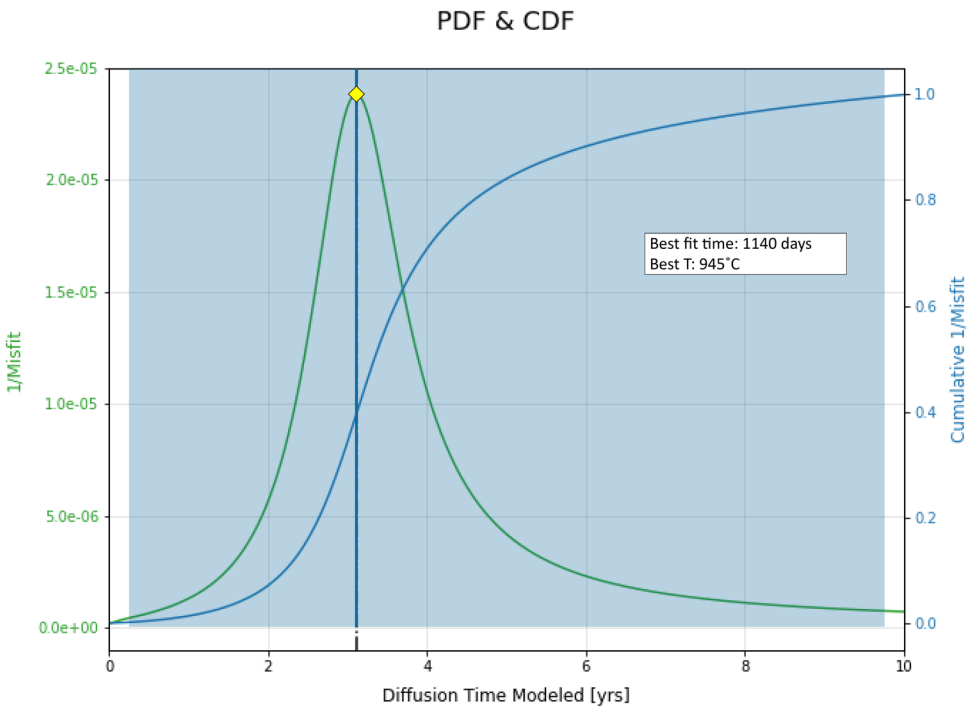

Fig. 6 Plot showing the inverse of the misfit of a diffusion modeling trial. The green line represents the probability distribution function, where the peak represents the best fit time of the model (yellow diamond). The blue plotted line is the cumulative distribution function, where misfit is summed and normalized to 1 to represent the low misfit range of times produced by the model. The transparent blue area represents the resulting 2σ confidence intervals (95% probability) calculated for the best fit time (vertical blue line)

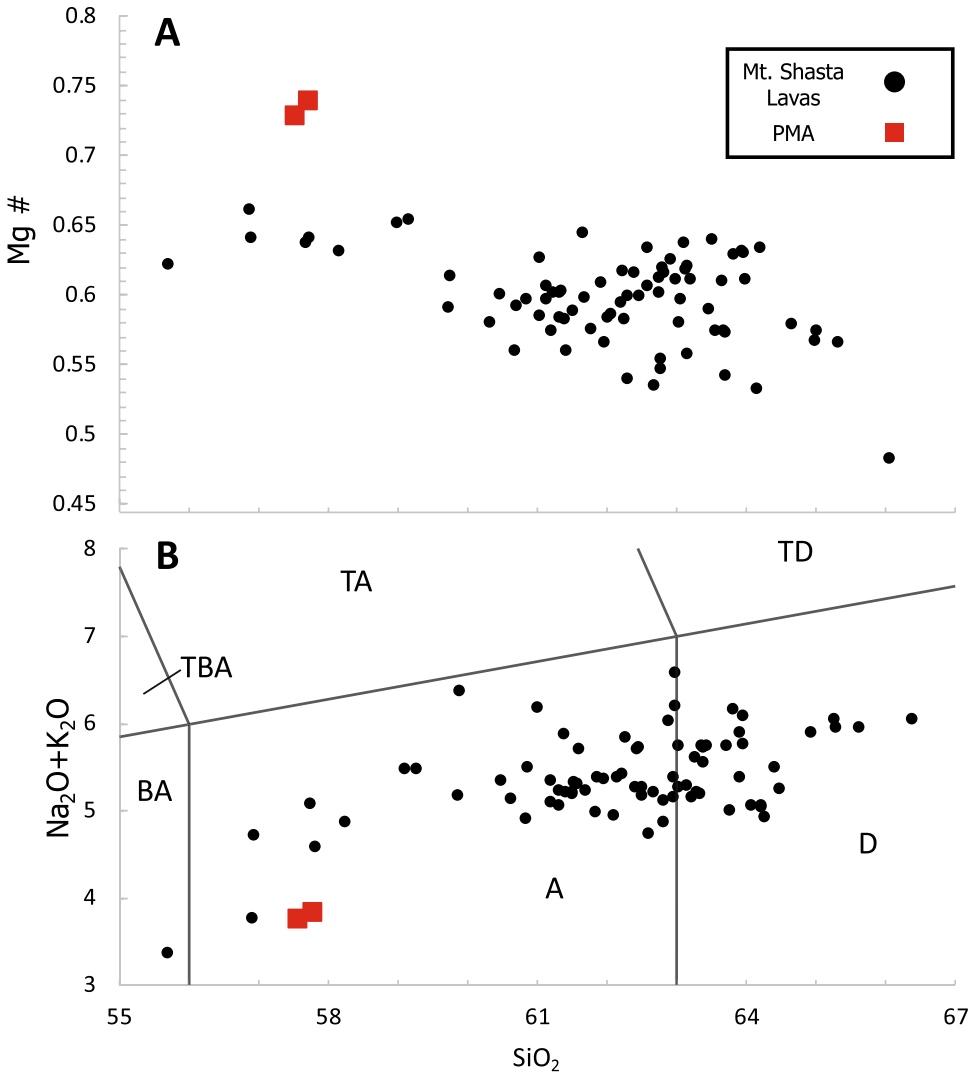

Fig. 7 Bulk geochemistry plots of PMA (red squares) compared to other Mt. Shasta lavas (black circles) (Grove et al. 2005). **A** Mg# vs. SiO_2 **B** Total alkalis vs. SiO_2; *BA* basaltic andesite, *A* andesite, *D* dacite, *TD* trachy-dacite, *TA* trachy-andesite, *TBA* trachy-basaltic andesite

element compositions and textural relationships (Fig. 9; Tables 5; 6): zoned pyroxenes with simple cores, zoned pyroxenes with resorbed cores, unzoned pyroxene, zoned olivine and skeletal olivine. The growth of a ubiquitous Mg-rich outer zone on all zoned pyroxene phenocrysts marked the beginning of modeled timescales and ascent rates. Some opx phenocrysts display resorption textures, such as sieve textures and sub-hedral crystal habits. There are also a small number of opx phenocrysts with clear oscillatory zoning. In these cases, only the outer-most zone was considered during diffusion modeling. Large (3–10 mm), euhedral, unzoned olivine, euhedral to sub-hedral unzoned clinopyroxene, and skeletal olivine are also present, having joined the crystallizing phase assemblage at various points of ascent, as described in Sect. 5.1. Notably, the occurrence of skeletal olivine crystals suggests some crystallization occurred between magma mixing and rim growth and ascent. Skeletal olivines are more Fe-rich than the large, olivine phenocrysts, suggesting they crystallized after more magma fractionation than the phenocrysts. The phase diagram indicates olivine leaving the crystallizing assemblage around 960 °C at the relevant pressures, so the skeletal olivine must have grown on the brink of metastability and quickly during ascent as suggested by their textures.

Thermobarometry and phase equilibrium experiments

As discussed in Sect. 2 above, the PMA crystallization conditions are well constrained by prior phase equilibria experiments (Grove et al. 2003; Krawczynski et al. 2012). The phase assemblage and major element comparisons of the natural pyroxene rim compositions very closely match the pyroxene major element compositions from experiment 41–107b in Krawczysnki et al. (2012) conducted at 975 °C and 500 MPa (Table 1); the average major element composition of both opx and cpx rims of all oxides are < 1 wt% different (with an average 0.37 wt% difference for cpx and

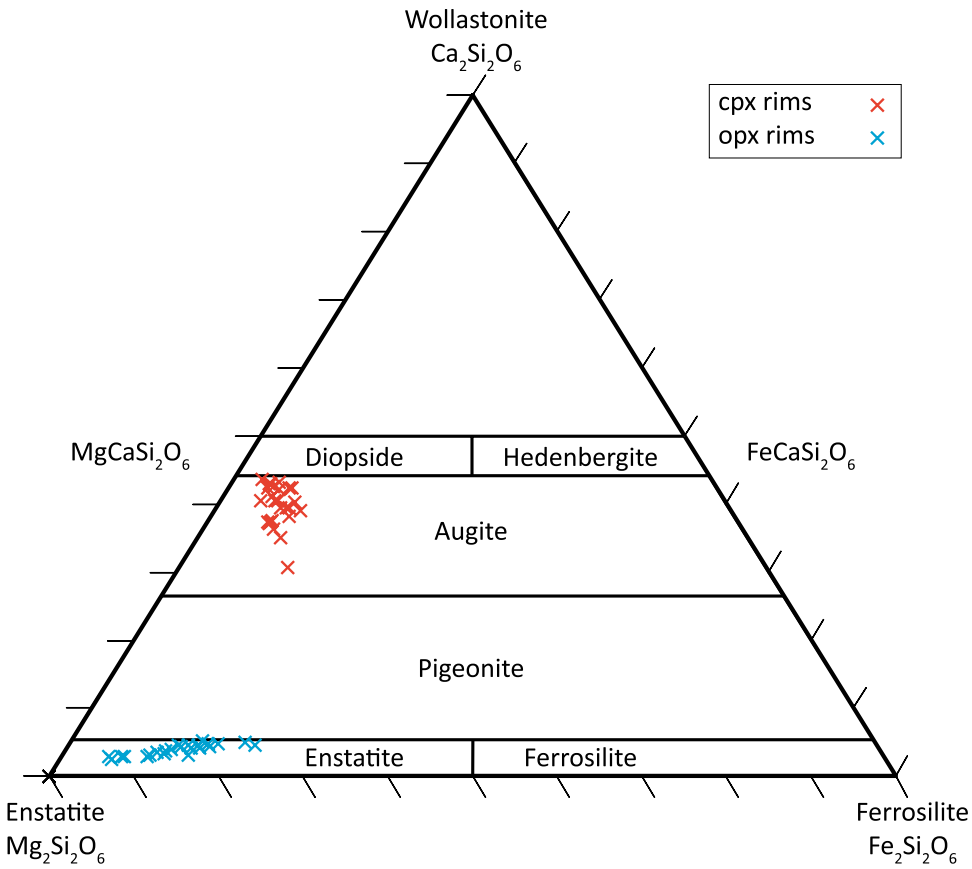

Fig. 8 Pyroxene ternary diagram showing clinopyroxene (red) and orthopyroxene (blue) rim compositions

0.25 wt% for opx) from those in 41–107b which matches the phase assemblage, as well as for those in 41–119b at the same *P–T* conditions but a higher fO_2 than deemed appropriate for the PMA. The same phase assemblage found in the PMA is stable over a range from 380 to 500 MPa and a range of ~ 40 °C in the experiments, which we use as the permissible ranges for uncertainty on the best *P–T* estimates from the experiments. The absolute pressure and temperature constraints and their corresponding uncertainty from experiments closely match those from the Putirka (2008) two pyroxene thermobarometer when applied to the pyroxene rims, which returns a pressure–temperature range of 260–670 MPa (± 377 MPa) using Eq. 38 and 925–1100 °C (± 60 °C) using Eq. 37, suggesting mid-crustal crystallization of the PMA at depths of ~ 7–20 km. Krawczynski et al. (2012) experiment 41c–107b also contains olivine, which is also present in the PMA but does not share the same consistent overgrowth textures as the pyroxene phenocrysts. The phase diagram produced by Krawczynski et al. (2012) illustrates that olivine-out occurs at ~ 950–970 °C between 380 and 500 MPa, such that crystallization and cooling move the PMA liquid out of the olivine stability field very quickly, thereby explaining the textural features we observe in the PMA olivine as well (Fig. 10). Therefore, the entire phase assemblage of the natural PMA and a subset of the experiments of Krawczynski et al. (2012) match quite well and were used to constrain the conditions used during diffusion modeling and subsequently for assessing ascent rates.

Diffusion chronometry timescales

The best fit time–temperature pair for each modeled cpx and opx grayscale profile (1 per phenocryst) that produced the lowest root mean squared misfit are reported in Table 3. Each of these individual profile results are like the result shown on the misfit contour plot in Fig. 5, in that it represents the singular temperature and diffusion variables that produced the lowest mean squared misfit but can be contextualized within a misfit map plotted in temperature vs. time that shows how misfit and thus error varies in this space overall. When averaged, these profiles reveal average best fit temperature–time pairs of $2.9^{+6.6}_{-2.7}$ years at 923 °C and $2.9^{+6.4}_{-2.2}$ years at 940 °C, for Fe–Mg interdiffusion in clinopyroxene and orthopyroxene, respectively (errors represent 95% confidence intervals) (Fig. 11, Table 3). The best fit temperatures returned by our Monte Carlo modeling approach are withing 7 °C of one another and within error of the best fit temperature from the experiments (975 ± 40 °C) and thermometry (925 ± 60 °C), which we take to confirm they record the same set of events at the same *P–T* conditions. If the results

Table 4 All olivine compositions

Sample	SiO_2	TiO_2	Al_2O_3	Cr_2O_3	FeO	MnO	MgO	CaO	Na_2O	K_2O	Total	Mg#
Subhedral olivine phenocrysts												
01-olv1	40.8303	0	0.005543	0.063665	8.02005	0.133935	50.645	0.122964	0	0.011379	99.8257	0.918399449
	40.8828	0.01563	0.009505	0.063059	8.44964	0.113678	50.346	0.123093	0.004311	0.017628	100.025	0.913938088
	40.7324	0.016038	0.017743	0.041807	7.97576	0.132475	50.3604	0.130328	0	0.009673	99.402	0.918392131
	41.0407	0.019174	0.008158	0.057231	7.88998	0.114891	51.0732	0.130903	0	0.021625	100.354	0.920236658
	40.8442	0.005857	0	0.039737	8.71627	0.101135	50.0627	0.124742	0	0.006739	99.88	0.911006393
	40.86608	0.0113398	0.0081898	0.0530998	8.21034	0.1192228	50.49746	0.126406	0.0008622	0.0134088	99.88	0.916401519
	40.86608	0.0113398	0.0081898	0.0530998	8.21034	0.1192228	50.49746	0.126406	0.0008622	0.0134088	99.89445	0.916395706
04-olv1*	40.6358	0.001772	0.006506	0.022497	13.6675	0.195148	44.7567	0.200538	0.00464	0.008069	99.49917	0.85372503
	40.8336	0.018934	0.023592	0.035094	13.2729	0.211398	45.3578	0.197514	0.004114	0.001731	99.956677	0.858969635
	40.5949	0.007687	0.012918	0.022859	13.5932	0.226684	45.0861	0.191542	0	0.023158	99.759048	0.855314261
	40.8212	0.010664	0.013954	0.037199	12.7123	0.201355	46.116	0.169048	0.03293	0.010479	100.125129	0.866051675
	41.2245	0.019311	0	0.028819	11.5	0.175222	46.8098	0.186923	0	0.011158	99.955733	0.878856528
	41.218	0.004753	0	0.053454	11.2504	0.186769	46.5253	0.188774	0.242158	0.025615	99.695223	0.880533621
	41.1503	0.009207	0.008714	0.04012	11.2516	0.150061	47.2183	0.160521	0	0.007518	99.996341	0.882069121
	41.2338	0	0.00516	0.04938	11.2152	0.165463	47.2865	0.164185	0.001213	0.020314	100.141215	0.882555459
	41.2836	0	0	0.039763	11.2337	0.13233	47.3702	0.156829	0	0.014862	100.231284	0.882567928
	41.2928	0.006531	0.01002	0.043152	11.125	0.197882	47.2873	0.165377	0	0.019403	100.147465	0.883391622
	41.3532	0.004454	0	0.02765	11.0884	0.161583	47.2695	0.157174	0	0.010653	100.072614	0.883691955
	41.3686	0	0.007917	0.039077	11.2024	0.140105	47.3797	0.160849	0.005283	0.006024	100.309955	0.882877533
	41.2877	0.000297	0	0.037897	11.0784	0.160597	47.2874	0.163809	0.000857	0.008002	100.024959	0.883823538
	41.3446	0.008296	0.00428	0.037675	11.225	0.166859	47.2669	0.152678	0	0.011456	100.217744	0.882421889
	41.3201	0	0.004177	0.036814	11.2128	0.177459	47.2065	0.154979	0.011571	0.008979	100.133379	0.882402048
	41.1778	0.010949	0.006481	0.035938	11.3052	0.128921	47.1192	0.167092	0	0.003787	99.955368	0.881354338
	41.3723	0.00444	0	0.028568	11.1817	0.17118	47.1269	0.157769	0.000952	0.008893	100.052702	0.882515092
	41.3059	0.001775	0	0.037257	11.3941	0.158119	47.1229	0.152902	0	0.005678	100.178631	0.880541072
	41.1736	0	0.002436	0.040042	11.675	0.177514	46.9533	0.159333	0	0.012251	100.193476	0.877568599
	41.2206	0.000295	0.00876	0.030495	11.6187	0.17637	46.6554	0.15206	0	0.009292	99.871972	0.877404023
	40.8256	0.007102	0.000817	0.032357	11.9284	0.190885	46.133	0.152251	0.007295	0.014663	99.29237	0.873305523
	42.1366	0.006812	0.031487	0.027498	12.5461	0.181344	46.4018	0.158887	0	0.015507	101.506035	0.868279218
	41.0594	0	0	0.030685	12.3446	0.156495	46.3007	0.15991	0	0.015672	100.067462	0.869873293
	41.0634	0.007712	0.008449	0.034125	11.8474	0.133918	46.5912	0.171706	0	0.020224	99.878134	0.875141425
	41.5262	0.016028	0.170574	0.018191	11.4244	0.195082	46.768	0.199538	0.020055	0.01577	100.353838	0.879462323
	41.483	0.004456	0.000927	0.022279	10.9463	0.205181	47.5426	0.159126	0.001791	0.009749	100.375409	0.885596039
	41.5337	0.006844	0.004749	0.034188	10.3969	0.126664	47.8474	0.131768	0	0	100.082213	0.891331035
	41.6299	0	0.012948	0.045156	9.71221	0.138327	48.376	0.129951	0.017527	0.004801	100.06682	0.898759856
	41.7114	0	0.006074	0.058751	9.5848	0.152171	48.6937	0.123048	0.002536	0	100.33248	0.900542926

Table 4 (continued)

Sample	SiO_2	TiO_2	Al_2O_3	Cr_2O_3	FeO	MnO	MgO	CaO	Na_2O	K_2O	Total	Mg#
	41.8434	0.002088	0	0.066736	9.10353	0.138698	49.1491	0.122626	0.008832	0.009939	100.444949	0.905859583
	41.8578	0	0	0.065464	8.72221	0.119092	49.1975	0.126007	0	0.014414	100.102487	0.909526794
	41.8666	0	0.010974	0.078309	8.47707	0.120783	49.4627	0.117349	0.004217	0.007704	100.145706	0.912276599
	42.0229	0.004479	0.006096	0.094646	8.1366	0.14685	49.7479	0.149457	0	0.007703	100.316631	0.91594588
	42.0252	0.011357	0.003981	0.073747	7.84406	0.126138	50.137	0.126957	0	0.010278	100.358718	0.919302175
	42.2766	0.001196	0	0.081192	7.61604	0.089138	50.2852	0.137148	0	0.015255	100.501769	0.921677092
	42.1275	0	0	0.076962	7.4035	0.113613	50.3547	0.119061	0	0.013847	100.209183	0.923793349
	42.1281	0	0.001745	0.074063	7.2693	0.098448	50.4962	0.120883	0	0	100.188739	0.925265483
	42.3785	0.005086	0	0.079094	7.15436	0.102687	50.6235	0.136483	0.004221	0.004726	100.488657	0.926531717
08-olv1**	39.2944	0.014036	0.194757	0.016019	17.0392	0.233378	40.692	0.232579	0.018425	0.009774	97.744568	0.809754457
	40.6953	0	0.017515	0.03197	10.8704	0.139508	48.1251	0.103905	0	0.009894	99.993592	0.887520529
	40.6905	0.016082	0.011457	0.031648	9.74093	0.122107	48.8268	0.135047	0	0.010316	99.584887	0.899333721
	40.7602	0.003525	0.01689	0.026506	8.71405	0.12859	49.9891	0.130552	0	0	99.769413	0.910907717
	40.7991	0.014111	0.013053	0.034287	8.31469	0.128677	50.4079	0.129241	0	0	99.841059	0.915291344
08-olv2*	42.394	0.090377	0.254857	0.042543	16.753	0.244927	39.8394	1.15771	0	0.032568	100.809382	0.809101049
	39.707	0.005418	0.023375	0.037416	14.4915	0.210939	44.894	0.190652	0.010254	0.010979	99.581533	0.84666012
	40.3519	0	0.039043	0.041823	11.9828	0.18598	47.3059	0.182306	0	0.005595	100.095347	0.875562536
	39.6848	0.021238	0.12458	0.054124	11.8962	0.183618	44.9851	0.186157	0	0.017498	97.153315	0.870795738
	33.653	0.04018	0.404971	0.035846	12.0247	0.182908	37.9826	0.328827	0.000149	0.026331	84.679512	0.849164854
	45.6214	0.378084	3.09985	0.035167	12.2955	0.206995	37.9678	1.59474	0.454644	0.277617	101.931797	0.846239425
	40.5699	0.031703	0.235692	0.04313	13.1223	0.199374	45.4871	0.25989	0.021333	0.031392	100.001814	0.860688024
	40.7334	0	0.00909	0.067573	12.3005	0.196149	47.084	0.164797	0.005089	0.011128	100.571726	0.872160053
	40.3258	0.022007	0.007107	0.049493	12.4163	0.177989	46.4959	0.164467	0	0.008907	99.66797	0.869693849
	40.4442	0.002054	0.007892	0.044354	12.2258	0.163626	46.63	0.148667	0.005819	0.002941	99.675353	0.871758384
	36.6125	0.031276	0.585057	0.033666	12.1145	0.155446	40.1553	0.183119	0.009372	0.011486	89.891722	0.855233435
	40.5258	0.01145	0.007913	0.052951	11.5789	0.166792	47.2485	0.129659	0.006557	0.007844	99.736366	0.879121477
	41.0504	0.004418	0.001313	0.053638	10.2236	0.163418	48.1583	0.131195	0	0.007532	99.793814	0.893566015
	39.9848	0.007087	0	0.08507	8.97117	0.092497	47.6309	0.128399	0.011538	0.00492	96.916381	0.904423103
	41.4491	0	0.00782	0.081165	8.02718	0.112768	50.1635	0.118956	0.000808	0.00345	99.964747	0.917613519
	41.4898	0.015414	0.000519	0.088836	7.482	0.086937	50.6769	0.121769	0	0.005917	99.968092	0.923499332
08-olv3**	41.4255	0.110309	0.323295	0.01797	17.4456	0.261957	41.4663	1.06383	0.02096	0.00997	102.145691	0.809026058
	40.2958	0.000871	0.000128	0.029943	11.7027	0.189248	47.4814	0.170668	0	0.004925	99.875683	0.878512528
	40.3497	0.011318	0	0.028477	11.5737	0.197654	47.7218	0.156027	0.004903	0.013727	100.057306	0.880224053
	40.2508	0.009278	0.00062	0.039267	11.9491	0.156307	47.5509	0.14346	0	0.016866	100.116598	0.876429596
	40.3752	0	0.016125	0.044993	12.0039	0.194742	47.512	0.147095	0.007564	0.004195	100.305814	0.87584423
	40.8882	0.008741	0.010949	0.061736	9.91087	0.135954	49.3841	0.136568	0	0.008904	100.546022	0.898794101

Table 4 (continued)

Sample	SiO_2	TiO_2	Al_2O_3	Cr_2O_3	FeO	MnO	MgO	CaO	Na_2O	K_2O	Total	Mg#
	40.7847	0	0	0.07908	9.61026	0.146676	49.3557	0.140844	0	0.005667	100.122927	0.90151057
	40.4523	0	0.001511	0.083986	11.5996	0.169409	47.7246	0.162858	0	0.006369	100.200633	0.879994378
	49.2319	0.282043	16.2068	0.049283	7.02574	0.153626	8.10846	7.48881	2.59801	0.159596	91.304268	0.672877367
Sample	SiO_2	TiO_2	Al_2O_3	Cr_2O_3	FeO	MnO	MgO	CaO	Na2O	K2O	TOTAL	Mg#
Skeletal olivine												
04-solv1*	54.9851	0.255045	7.63865	0.026496	11.4302	0.286164	19.3025	5.44394	1.58439	0.173239	101.125724	0.750611484
	54.7156	0.195894	1.02102	0.046245	11.4998	0.289794	27.6878	4.0946	0.032068	0.012642	99.595463	0.8110064
	39.9143	0.072381	0.215751	0.014337	15.1102	0.218654	43.7384	0.306395	0.011731	0.030734	99.632883	0.837637913
	40.3417	0.00943	0.02062	0.034498	12.773	0.194984	46.5157	0.189229	0	0.01584	100.095001	0.866499566
	40.3315	0.001476	0.020945	0.043163	11.8818	0.191075	47.4368	0.199254	0	0.014127	100.12014	0.876780681
04-solv2*	52.7071	0.140673	0.973586	0.07877	11.1011	0.241274	26.6671	3.13484	0.038404	0.031491	95.114338	0.810657323
	39.3194	0.022727	0.162357	0.010622	16.1624	0.223711	43.3782	0.308419	0.027592	0.010332	99.62576	0.827093964
	38.1326	0.014666	0.206802	0.029797	12.9203	0.195136	42.9824	0.196831	0.012829	0.030983	94.722344	0.855683476
	40.2937	0	0.021166	0.019531	11.8525	0.17469	47.0528	0.159963	0.001097	0.005657	99.581104	0.876168008
	40.2606	0.021491	0.016479	0.044225	11.7932	0.173739	47.3389	0.172367	0	0.017204	99.838205	0.877364913
	40.4381	0.009419	0	0.032381	11.6784	0.205498	47.5125	0.16436	0	0.014415	100.055073	0.878803956
04-solv3*	53.873	0.29921	1.24852	0.116132	9.38959	0.285908	23.0324	10.6926	0.148032	0.02695	99.112342	0.813846602
	52.6933	0.195453	1.02594	0.083156	11.2928	0.253937	29.9642	3.55162	0.055715	0.06438	99.180501	0.825453037
	54.5222	0.224511	1.14567	0.091296	11.075	0.235471	27.664	5.46615	0.060425	0	100.484723	0.816579384
	42.8804	0.097799	0.548348	0.039011	12.9933	0.222994	40.3977	1.69747	0.033237	0.030774	98.941033	0.847126541
	40.2147	0.013751	0	0.041657	13.1267	0.183505	45.862	0.174808	0	0.012555	99.629676	0.861629336
	40.5483	0.004983	0.016951	0.032527	12.3028	0.167895	46.6397	0.157643	0.005796	0.000571	99.877166	0.871078206
	40.6818	0.013788	0.025482	0.035588	11.8093	0.182516	46.9576	0.168264	0	0.003347	99.877685	0.876344333
08-solv1*	56.1471	0.176091	0.945208	0.121325	10.7028	0.24615	29.7429	2.2421	0.01897	0.00089	100.343534	0.832016374
	57.5191	0.081273	1.30494	0.606164	5.71482	0.140041	33.9897	1.69746	0.033643	0.003104	101.090245	0.913796356
	57.8649	0.06537	1.16703	0.804161	4.65312	0.110827	35.1406	1.36853	0.040929	0.005652	101.221119	0.930843541
	57.2176	0.068241	1.47638	1.19506	4.77308	0.121853	34.3955	1.72979	0.024704	0.017645	101.019853	0.927763708
	56.9024	0.075035	1.60923	1.42087	4.51764	0.10801	34.3452	1.73789	0.042739	0.005471	100.764485	0.931270616
08-solv2**	40.8122	0.010714	0.006969	0.039587	11.4997	0.15036	47.0931	0.153358	0.006956	0.023446	99.79639	0.879500243
	40.3848	0.002018	0	0.016947	12.894	0.200194	45.8358	0.152771	0	0.013334	99.499864	0.863680783
	40.8584	0.00376	0.001817	0.029016	11.8319	0.179897	46.7588	0.145167	0	0.009903	99.81866	0.875675854
	40.4923	0.004329	0.021475	0.03755	12.5612	0.172539	46.1549	0.177226	0	0.015189	99.636708	0.867529667
08-solv3**	40.4847	0	0	0.041414	12.1019	0.176149	46.9123	0.137045	0.021288	0.00829	99.883086	0.873561001
	40.5538	0	0.000206	0.022098	11.8906	0.164606	46.8401	0.149926	0	0	99.621336	0.875325782
11-solv1**	39.9214	0	0.00692	0.024636	11.4827	0.179796	46.9602	0.161415	0	0.01021	98.7495	0.879357451

Table 4 (continued)

Sample	SiO_2	TiO_2	Al_2O_3	Cr_2O_3	FeO	MnO	MgO	CaO	Na2O	K2O	TOTAL	Mg#
	40.5487	0	0.007781	0.050091	12.1683	0.149528	47.3755	0.144669	0.008455	0.026675	100.47	0.874041081
	40.5842	0	0.008247	0.030302	11.3859	0.20265	47.7194	0.158237	0	0.007238	100.078	0.881932896
	40.6056	0	0.012646	0.032333	12.0287	0.14341	47.5297	0.142267	0	0.012621	100.499	0.875660189
	40.058	0	0.025537	0.021948	14.7582	0.22971	44.9742	0.166569	0	0.002241	100.222	0.844512039
	40.6376	0.00617	0	0.037338	11.4958	0.133368	47.7608	0.163552	0	0.007157	100.236	0.881019906
	39.915	0.017944	0.074177	0.011967	15.7447	0.238901	44.2343	0.301498	0.013703	0.021735	100.574	0.833535922
12-solv1	40.7283	0	0.000742	0.041621	11.431	0.181473	46.8079	0.158666	0.008066	0.009484	99.367252	0.879491497
12-solv2*	41.9913	0.020822	0.108929	0.017478	15.4143	0.19428	43.4036	0.408297	0.001531	0.009078	101.569615	0.833847888
	40.1878	0.013259	0.029228	0.04029	13.0598	0.168156	45.8624	0.18946	0.000585	0.007306	99.558284	0.862238425
	40.9553	0.010342	0	0.026963	11.9184	0.191343	47.1429	0.169194	0	0.002056	100.416498	0.875773452
	40.9173	0	0.01604	0.031652	11.7684	0.18067	47.343	0.16054	0	0.007152	100.424754	0.877600539
	40.736	0	0.021932	0.026626	11.7157	0.142202	47.3272	0.1626	0.00167	0.013726	100.147656	0.878046092
	40.8124	0.000295	0.00244	0.029801	11.7287	0.149376	47.4253	0.159957	0.007495	0.008381	100.324145	0.878149029
	40.2316	0.003838	0.005763	0.036832	11.478	0.148265	46.9396	0.157992	0.009507	0.009282	99.020679	0.879354335
	40.799	0.008272	0.006987	0.038403	11.2184	0.134372	47.5688	0.15557	0.021021	0.011094	99.961919	0.883141574
	40.9532	0.00827	0.048525	0.041079	11.2454	0.15555	47.5469	0.187307	0.02271	0.004764	100.213705	0.88284564
	40.9758	0	0.014672	0.033725	10.9319	0.159421	47.8617	0.152383	0	0.000575	100.130176	0.886404655
	40.9284	0	0.023672	0.043477	10.6953	0.15291	48.0997	0.132333	0	0.008869	100.084661	0.889079418
	41.0246	0.001183	0.005323	0.033661	10.1761	0.158877	48.4786	0.129239	0	0.006986	100.014569	0.894634612
	41.1105	0.012132	0.015758	0.038767	9.81227	0.123031	48.7813	0.126674	0.007843	0.005426	100.033701	0.898586245
	41.1491	0.00148	0.005228	0.052994	9.47061	0.119198	49.0465	0.134329	0	0.018828	99.998267	0.90224979
	41.426	0.00681	0	0.071949	9.31629	0.113642	49.3199	0.124481	0.002687	0.010032	100.391791	0.904171916
	41.2918	0.013037	0	0.050915	8.93894	0.139548	49.4319	0.136941	0	0.001974	100.005055	0.907884965
	41.4461	0	0.006095	0.054134	8.84019	0.135029	49.5739	0.128052	0.003639	0.013239	100.200378	0.909047228
	41.354	0.014214	0	0.054454	8.81761	0.103928	49.7051	0.134818	0	0.004849	100.188973	0.9094763
	41.3772	0.005922	0	0.074944	8.66747	0.131302	49.5115	0.126624	0	0.013479	99.908441	0.910562997
12-solv3*	54.5699	0.296811	1.3167	0.108093	10.5285	0.312249	25.1455	7.04918	0.088719	0.022567	99.438219	0.809766496
	55.098	0.230281	1.14304	0.106721	11.1631	0.303754	27.1668	4.40978	0.07731	0.01735	99.716136	0.812643988
	52.1403	0.23228	1.37894	0.123393	11.0298	0.240138	30.6945	2.45932	0.023588	0.014847	98.337106	0.832211637
	40.5835	0.008755	0.008502	0.021951	12.7476	0.189151	46.1526	0.175867	0	0.009592	99.897518	0.865821857
	40.6208	0.005262	0.009683	0.028324	11.9727	0.202622	46.6717	0.165856	0.01199	0.014648	99.703585	0.874177304
	40.7833	0.0117	0.019949	0.026199	11.8101	0.203727	47.0561	0.172266	0	0.005698	100.089039	0.876563897
	40.6888	0.009943	0	0.034816	11.7589	0.185494	47.0355	0.149085	0	0.000814	99.863352	0.876985993
12-solv4*	40.202	0.022464	0.099911	0.060089	17.3278	0.227528	41.2879	0.310147	0	0.004911	99.54275	0.809406424
	40.5839	0	0.003453	0.06968	12.3139	0.165839	46.046	0.170352	0.005954	0.012265	99.371343	0.869530366
	41.0839	0.014608	0.020741	0.080025	11.7188	0.164977	47.02	0.161832	0.0118	0.01618	100.292863	0.877318573

Table 4 (continued)

Sample	SiO_2	TiO_2	Al_2O_3	Cr_2O_3	FeO	MnO	MgO	CaO	Na2O	K2O	TOTAL	Mg#
22-solv1**	55.9515	0.17375	0.944113	0.101906	10.3742	0.287715	27.979	4.26664	0.042824	0.010676	100.132324	
	41.2004	0	0.005575	0.037373	11.3571	0.153672	47.2699	0.148875	0	0.005072	100.177967	
	41.0714	0	0.015591	0.055837	11.9149	0.14782	47.1138	0.143935	0	0.002116	100.465399	
22-solv2*	42.0241	0.034192	0.191084	0.019047	15.7207	0.228821	42.0719	0.523982	0	0.010895	100.824721	
	40.4118	0	0.002869	0.028948	13.3329	0.190649	45.6328	0.180671	0	0.01243	99.793067	
	40.9474	0.003783	0.018232	0.032817	11.9004	0.162052	47.0504	0.164102	0.009712	0.015467	100.304365	
	41.1143	0.014525	0	0.039545	11.657	0.186071	47.454	0.152373	0	0.004769	100.622583	
	41.08	0	0.017386	0.038546	11.5456	0.165772	47.4985	0.151758	0	0.00913	100.506692	
	41.1532	0.002033	0	0.020267	11.3767	0.150984	47.4416	0.146823	0	0.006625	100.298232	
	41.2131	0	0.008155	0.023697	11.6254	0.175367	47.6959	0.147254	0.005319	0.000161	100.894353	

All compositions are reported from rim (top) to core (bottom)

*Transect

**Single points

from all of the cpx and opx profiles are averaged the event has a singular timescale of ~$2.9^{+6.4}_{-2.2}$ years.

Discussion

Magma mixing and storage history

Combining the petrographic, thermobarometric, and analytical geochemical results provides a framework for constructing a conceptual model of the volcanic plumbing system of the Mt. Shasta PMA. Our results suggest multiple mixing events occurred involving more and less evolved versions of the primitive PMA magma between 925–1100 °C and 260–670 MPa, or ~ 7–20 km. Notably, the presence of similar Mg-rich reverse zoning on multiple, compositionally unique pyroxene core populations suggests a mixing and growth step shared by nearly all pyroxene phenocrysts in the PMA. Evidence of a near compositional overlap between natural pyroxene rim compositions and experimentally derived pyroxenes from Krawczynski et al. (2012) narrow the likely Mg rich growth conditions to roughly 975 °C and 500 MPa (~ 15 km). Though multiple experiments, performed at roughly the same *P–T* conditions, contain pyroxene compositions that closely resemble the average rim composition of the natural PMA, only one displays an analogous phase assemblage. The experiment 41–107b similarly lacks amphibole and was conducted at NNO, rather than NNO + 3. Given the hydrous nature of the PMA, and its lack of amphibole, a less oxidized environment is likely. Our detailed petrography, mineral analyses thermobarometry, and experimental comparison suggests the following history that includes multiple mixing and growth events (Fig. 12): (A) Crystallization of clinopyroxene and orthopyroxene cores (Table 5). This step likely occurred after some amount of fractionation given the higher FeO content of all core populations. (B) Mid-crustal mixing of variably fractionated versions of the PMA containing the pyroxene nuclei. Some of the more complex textures such as minor resorption and oscillatory zoning of some orthopyroxene cores occurs during this step. (C) An injection of a more primitive, Mg-rich version of the PMA containing other pyroxene phenocrysts and large, unzoned olivine phenocrysts mixed with the other two crystal populations and subsequently caused the crystallization of the Mg-rich pyroxene rims at ~ 15 km depth (Table 6). The large olivine phenocrysts from this step do contain some core to rim fractionation distinct from the reverse zoning of the pyroxene phenocrysts. However, these olivines do share a thing, outer Fe rich rim, similar to all other phenocrysts. (D) Ascent of the now hotter and relatively homogenous magma causes decompression and

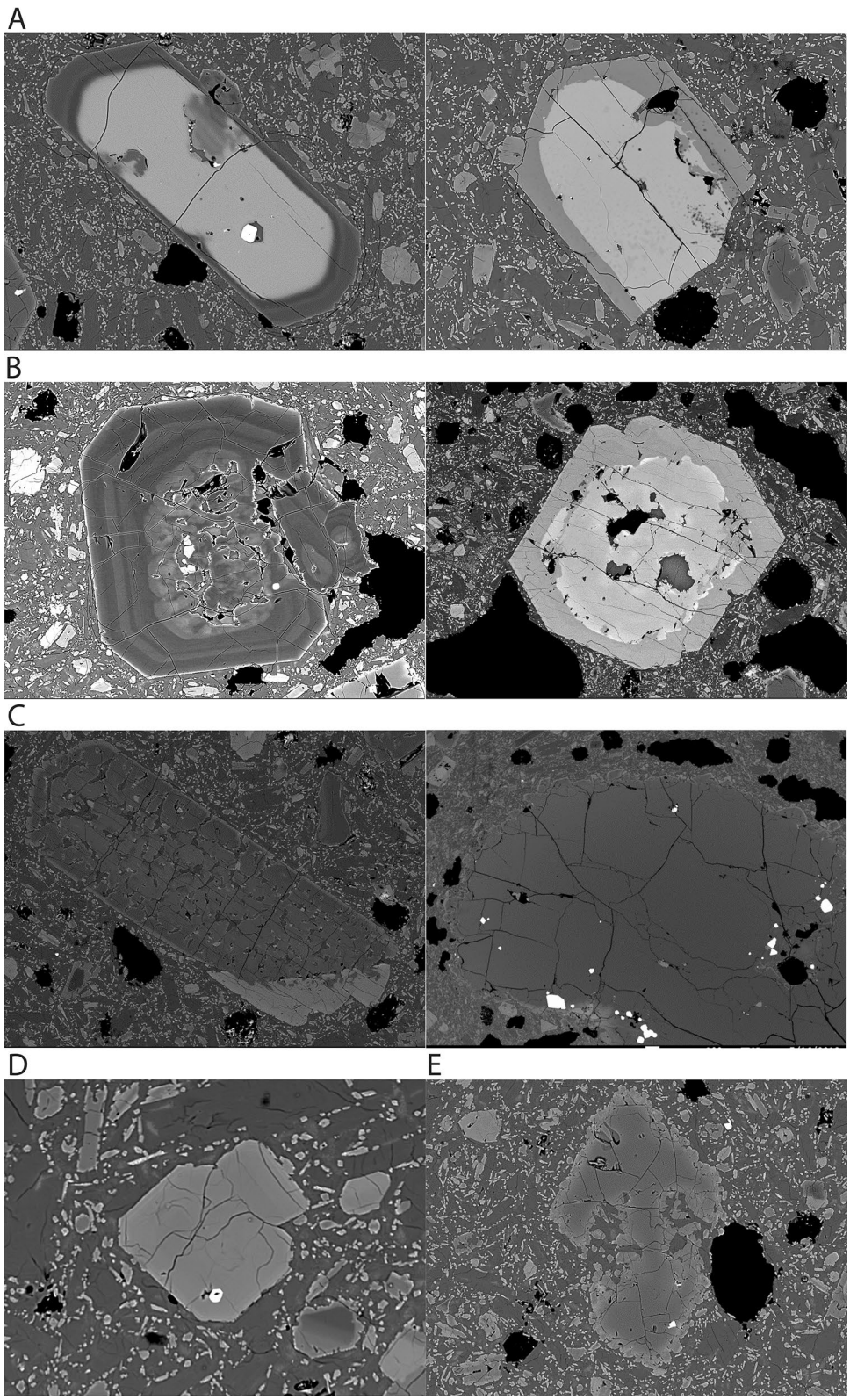

Fig. 9 BSE images of phase populations. **A** population 1 pyroxenes with simple cores (opx left; cpx right). **B** population 2 pyroxenes with resorbed cores (opx left; cpx right). **C** phases from the Mg-rich recharge (opx left; ol right). **D** unzoned cpx. **E** skeletal olivine

undercooling, leading to the crystallization of new, unzoned clinopyroxene phenocrysts. In the very early stages of ascent, skeletal olivine crystals likely grew on the brink of metastability before the *P–T* conditions of the ascending magma exited the olivine stability field (Fig. 9). Further fractionation during subsequent steps causes the growth of

Table 5 Representative major element compositional analyses of each pyroxene core

Sample	SiO_2	TiO_2	Al_2O_3	Cr_2O_3	FeO	MnO	MgO	CaO	Na_2O	K_2O
Pop. 1 cpx										
04-cpx1	51.20	0.53	2.49	0.35	9.78	0.23	14.27	19.96	0.43	0.01
04-cpx7	51.65	0.65	2.32	0.05	10.89	0.26	14.15	19.41	0.46	0.01
04-cpx8	53.60	0.37	1.79	0.21	7.79	0.22	17.97	18.38	0.24	0.01
01-cpx3	51.15	0.55	2.20	0.08	10.04	0.21	14.12	20.59	0.50	0.01
04-cpx6	51.35	0.64	1.89	0.05	11.11	0.28	13.93	19.40	0.33	0.01
08-cpx3	50.71	0.64	2.63	0.09	11.89	0.27	13.74	18.83	0.45	0.01
11-cpx1	51.66	0.59	2.17	0.08	10.96	0.24	14.59	19.28	0.44	0.01
11-cpx2	51.12	0.61	2.56	0.05	11.56	0.25	13.91	19.40	0.47	0.01
12-cpx1	52.28	0.55	2.70	0.43	5.37	0.14	16.43	21.03	0.42	0.01
16-cpx1	49.72	0.69	3.43	0.06	11.10	0.24	13.73	19.78	0.47	0.01
16-cpx2	54.25	0.19	1.78	0.54	4.44	0.13	19.17	20.19	0.25	0.01
16-cpx3	50.48	0.60	2.37	0.05	11.22	0.26	13.76	19.62	0.53	0.01
Pop. 2 cpx										
01-cpx1	52.55	0.34	2.28	0.22	7.92	0.20	17.55	18.42	0.35	0.01
11-cpx3	51.38	0.47	3.99	0.57	6.81	0.15	15.96	20.37	0.45	0.01
22-cpx1	53.50	0.37	2.05	0.13	8.68	0.21	16.81	18.39	0.36	0.01
01-cpx2	52.68	0.35	2.80	0.28	7.09	0.17	17.36	19.22	0.36	0.01
04-cpx4	52.77	0.34	1.96	0.30	6.50	0.17	18.07	19.13	0.25	0.01
04-cpx5	52.23	0.44	2.65	0.16	8.71	0.20	16.49	18.11	0.38	0.01
08-cpx1	52.92	0.33	2.18	0.17	7.46	0.20	17.92	17.98	0.29	0.01
08-cpx2	52.85	0.31	2.24	0.27	7.39	0.18	17.43	18.50	0.32	0.01
12-cpx4	52.59	0.38	1.78	0.15	8.59	0.22	17.77	17.58	0.25	0.01
12-cpx7	52.99	0.31	3.21	0.21	6.62	0.16	17.39	18.99	0.38	0.04
23-cpx1	52.91	0.44	2.26	0.12	9.71	0.23	16.32	18.03	0.39	0.01
Pop. 1 opx										
04-opx1	52.87	0.31	1.14	0.04	19.44	0.44	23.63	1.53	0.07	0.01
04-opx4	52.66	0.27	1.26	0.02	20.02	0.46	22.97	1.54	0.05	0.01
12-opx2	52.61	0.27	1.18	0.04	19.71	0.42	23.03	1.53	0.06	0.01
16-opx1	54.73	0.10	1.94	0.15	12.95	0.24	28.31	1.68	0.03	0.01
Pop. 2 opx										
04-opx3	55.07	0.16	1.03	0.05	13.06	0.29	28.29	1.86	0.05	0.02
11-opx1	54.41	0.14	2.31	0.08	11.75	0.23	29.07	1.72	0.04	0.01
22-opx3	57.37	0.15	1.07	0.14	9.35	0.22	30.35	2.09	0.04	0.02
Mg-rich recharge opx										
01-opx1	56.62	0.07	1.24	0.59	6.45	0.14	33.31	1.78	0.04	0.01
04-opx5	56.92	0.10	1.12	0.34	7.63	0.18	31.97	2.27	0.03	0.01
08-opx3	55.91	0.11	1.82	0.45	7.84	0.17	32.18	1.76	0.03	0.01
08-opx4	56.80	0.08	1.06	0.49	7.92	0.17	32.13	1.51	0.03	0.01
11-opx2	55.95	0.05	1.07	0.40	6.53	0.15	33.07	1.48	0.03	0.01
12-opx3	57.40	0.07	0.93	0.54	5.98	0.13	33.19	1.91	0.03	0.01
12-opx4	57.40	0.08	0.82	0.28	7.34	0.17	32.73	1.82	0.03	0.01
16-opx2	56.13	0.07	1.50	0.64	6.79	0.13	32.94	1.66	0.03	0.01
22-opx1	57.02	0.13	2.03	0.28	7.71	0.16	31.60	1.89	0.07	0.01

Different pyroxene populations are grouped by textural and compositional differences

thin, FeO rich rinds on nearly all phenocrysts. (5) Upon eruption, small groundmass phases such as pyroxene, olivine, and microlitic plagioclase are crystallized as the now lava cools.

Growth vs. diffusion

An important consideration when utilizing diffusion chronometry is determining the process responsible for

Table 6 Representative major element compositional analyses of each pyroxene rim

Sample	SiO_2	TiO_2	Al_2O_3	Cr_2O_3	FeO	MnO	MgO	CaO	Na_2O	K_2O
Pop. 1 cpx										
04-cpx1	53.29	0.20	1.88	1.02	4.11	0.11	18.50	20.53	0.36	0.01
04-cpx7	53.44	0.27	2.57	1.12	4.13	0.13	17.70	21.34	0.21	0.01
04-cpx8	54.20	0.21	2.03	1.03	4.04	0.14	18.90	20.56	0.23	0.01
01-cpx3	52.28	0.21	1.92	1.00	4.02	0.13	18.24	21.01	0.22	0.02
04-cpx6	53.35	0.21	2.13	1.05	3.78	0.09	17.81	20.99	0.25	0.01
08-cpx3	53.34	0.22	2.10	1.08	3.89	0.10	18.32	20.87	0.24	0.01
11-cpx1	53.33	0.22	1.93	0.94	3.93	0.15	18.50	21.17	0.18	
11-cpx2	52.91	0.35	3.19	0.54	4.71	0.13	17.94	20.53	0.37	0.01
12-cpx1	54.09	0.22	1.36	0.37	5.36	0.17	19.83	18.19	0.14	0.01
16-cpx1	52.36	0.23	2.17	1.14	4.04	0.11	18.12	21.38	0.23	0.01
16-cpx2	54.18	0.22	1.65	0.55	4.55	0.13	19.17	20.37	0.19	0.02
16-cpx3	52.51	0.32	2.11	0.52	4.80	0.15	17.59	20.80	0.28	0.07
Pop. 2 cpx										
01-cpx1	52.71	0.27	2.19	0.60	4.89	0.13	19.10	19.67	0.19	0.01
11-cpx3	53.54	0.21	1.98	1.05	4.11	0.13	18.81	20.45	0.22	0.01
22-cpx1	54.38	0.21	2.10	0.94	4.23	0.13	18.82	20.11	0.26	0.01
01-cpx2	53.05	0.25	2.29	1.01	4.15	0.09	18.55	20.65	0.24	0.01
04-cpx4	52.93	0.20	1.89	1.02	3.75	0.15	18.19	21.24	0.21	0.01
04-cpx5	53.08	0.22	2.13	1.19	3.94	0.12	18.10	20.72	0.27	0.02
08-cpx1	53.82	0.17	1.87	1.01	3.85	0.11	18.79	20.01	0.27	0.02
08-cpx2	53.29	0.21	1.92	0.98	4.29	0.10	18.82	19.62	0.23	0.01
12-cpx4	53.06	0.18	1.70	0.71	4.07	0.12	18.56	20.12	0.22	0.01
12-cpx7	53.57	0.21	1.98	0.89	4.07	0.12	18.50	20.42	0.22	0.01
23-cpx1	53.94	0.23	2.04	1.06	4.23	0.13	18.88	20.14	0.21	0.02
Pop. 1 opx										
04-opx1	56.89	0.08	1.53	1.02	5.36	0.13	33.97	1.58	0.04	0.01
04-opx4	57.10	0.05	1.52	0.88	5.34	0.12	33.61	1.63	0.07	0.02
12-opx2	56.91	0.07	1.57	0.90	5.37	0.11	33.64	1.54	0.03	0.01
16-opx1	57.09	0.07	1.46	0.75	5.21	0.14	34.29	1.58	0.03	0.01
Pop. 2 opx										
04-opx3	57.44	0.04	1.33	0.85	4.85	0.12	34.52	1.45	0.03	0.01
11-opx1	56.60	0.07	1.61	0.80	5.52	0.12	33.65	1.85	0.05	0.01
22-opx3	58.21	0.07	1.43	0.93	5.14	0.12	33.91	1.48	0.06	0.01
Mg-rich recharge opx										
01-opx1	56.77	0.07	0.98	0.58	5.71	0.14	34.05	1.43	0.02	0.01
04-opx5	57.43	0.09	1.49	0.68	6.71	0.15	32.82	1.97	0.04	0.02
08-opx3	56.53	0.08	1.43	0.70	6.42	0.16	33.37	1.63	0.03	0.01
08-opx4	56.76	0.09	1.53	0.61	6.78	0.14	32.79	1.61	0.03	0.01
11-opx2	55.91	0.07	1.25	0.79	4.80	0.12	34.33	1.42	0.03	0.02
12-opx3	56.63	0.11	1.48	0.49	7.26	0.13	32.29	1.55	0.03	0.00
12-opx4	57.27	0.11	1.11	0.39	6.74	0.17	33.10	1.77	0.03	0.02
16-opx2	56.42	0.08	0.93	0.40	6.46	0.11	32.67	2.15	0.04	0.01
22-opx1	57.03	0.13	1.99	0.27	7.66	0.17	31.70	1.88	0.04	

Different pyroxene populations are grouped by textural and compositional differences

producing the concentration profile observed in zoned minerals. The concentration profile can be the result of crystal growth during magma mixing ("growth"), elemental diffusion following magma mixing and crystal rim growth ("diffusion") or both happening on similar timescales ("growth + diffusion"). The distinction can be difficult to discern from BSE images alone. Instead, utilizing the

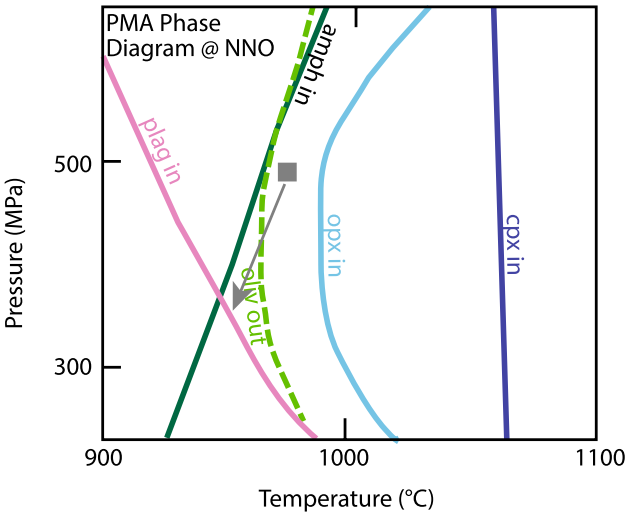

Fig. 10 Phase diagram showing stability fields of PMA phenocrysts. Cooling and depressurization (indicated by gray arrow) occurs during ascent and moves the PMA out of the olivine stability field, ceasing the growth of skeletal olivine phenocrysts. The lack of amphibole indicated *P–T* conditions did not enter the amphibole stability zone during ascent. Phase boundaries from Krawczynski et al. 2012. Gray square represents location of PMA in pressure–temperature space

concentration profiles of elements with different diffusivities (here we use Ca and Cr in addition to Fe and Mg) is useful to distinguish between the growth vs. diffusion mechanisms. If the profiles exhibit coupled behavior (i.e., similar concentration profile widths) between the elements with different diffusivities, crystal growth is likely the responsible mechanism (e.g., Shamloo and Till 2019; Till et al. 2015), whereas decoupled behavior between elements with different diffusivities is more consistent with diffusion being the dominant mechanism. In the PMA pyroxenes, we observe decoupled behavior of elements with different diffusivities; the Ca concentration profile is relatively flat compared to those of Mg and Fe, whereas the Cr profile is shorter and steeper than Mg and Fe (Fig. 13). minor amounts of Mn substituting for Mg in the Fe–Mg exchange reaction and atomic mass effects. These minor substitutions do not seem to affect the outcomes of diffusion modeling due to the low effect Mn substitution has on the overall brightness of BSE images. Therefore, we conclude diffusion is the dominant mechanism producing the concentration profiles between the outermost pyroxene rims and crystal interiors.

Ascent rates

Previously, the Mt. Shasta PMA was interpreted to have experienced rapid single-stage ascent from near the Moho to the surface (Grove et al. 2005). However, this work reveals a more complex multi-stage ascent for the PMA, including several mixing events between variably fractionated PMA liquids in the mid-crust. Though previous studies have estimated ascent rates for magmas transiting the entire crust ("trans-crustal ascent rates"), this study is one of the first to determine the timescales, and, therefore, ascent rates, from a specific event at a specific depth in the mid-crust to eruption, especially in an arc setting. As discussed above, we conclude the PMA experienced Mg-rich pyroxene rim growth at ~ 500 MPa (~ 15 km depth) less than 10 years, or more specifically ~$2.9^{+6.5}_{-2.5}$ years, before eruption. Using this best fit timescale and depth of mixing yields average upper-crustal ascent rates of ~ 5 km/year or a range of ~ 2–38 km/year (~ 5–100 m/day) using the 95% confidence interval on the best fit timescale. The minimum possible pressure (380 MPa, ~ 11.4 km) that produces the same phase assemblage as the PMA in the experiments, would yield an ascent rate of ~ 4 km/year using the best fit time, within the range of ascent rates produced by the timescale uncertainty. These ascent rates are minimum values, determined solely by the amount of time elapsed, since magma mixing occurred, likely catalyzing pyroxene rim growth and the initiation of magma ascent.

The PMA likely ascended more rapidly during the final syn-eruptive stage of ascent. The majority of studies of magma ascent rates focus on syn-eruptive rates, such as those captured by melt embayment volatile gradients (e.g., Lloyd et al. 2014), which report rates much faster than described by this study, on the order of 10^6 m/day. Le Voyer et al. (2010) found an average H_2O–CO_2 saturation pressure of ~ 100 MPa for the basaltic andesite (BA), another primitive hydrous magma at Mt. Shasta. While the BA has distinct origins from the PMA and a lower water content (Grove et al. 2003), if we assume a similar pressure for the onset of these syn-eruptive ascent rates, the PMA ascended would have ascended the last 100 MPa (~ 3 km), in less than a day. Prior to the onset of syn-eruptive rates, wherever their onset for the PMA, our work suggests the PMA travelled at a minimum constant rate of ~ 5 km/year or ~ 14 m/day. This average upper crustal ascent rate is useful for understanding longer term and perhaps average upper crustal magma flux.

The PMA mid-to-upper crustal ascent rate falls within the range of the trans-crustal ascent rate estimates, which range from ~ 1 to 3000 km/year (~ 2–8000 m/day) (Blatter and Carmichael 1998; Ruprecht and Plank 2013; Mutch et al. 2019; Hollyday et al. 2020) (Table 7). Rates at the faster end of this spectrum come from Iceland, where thinner lithosphere and extensional tectonic setting likely facilitate the fast ascent of mantle-derived magmas (e.g., Mutch et al. 2019), whereas the slower thicker lithosphere and the complex plumbing systems beneath a long-lived arc stratocones seem may contribute to the slower ascent of hydrous mafic arc magmas as observed here (e.g., Hollyday et al. 2020).

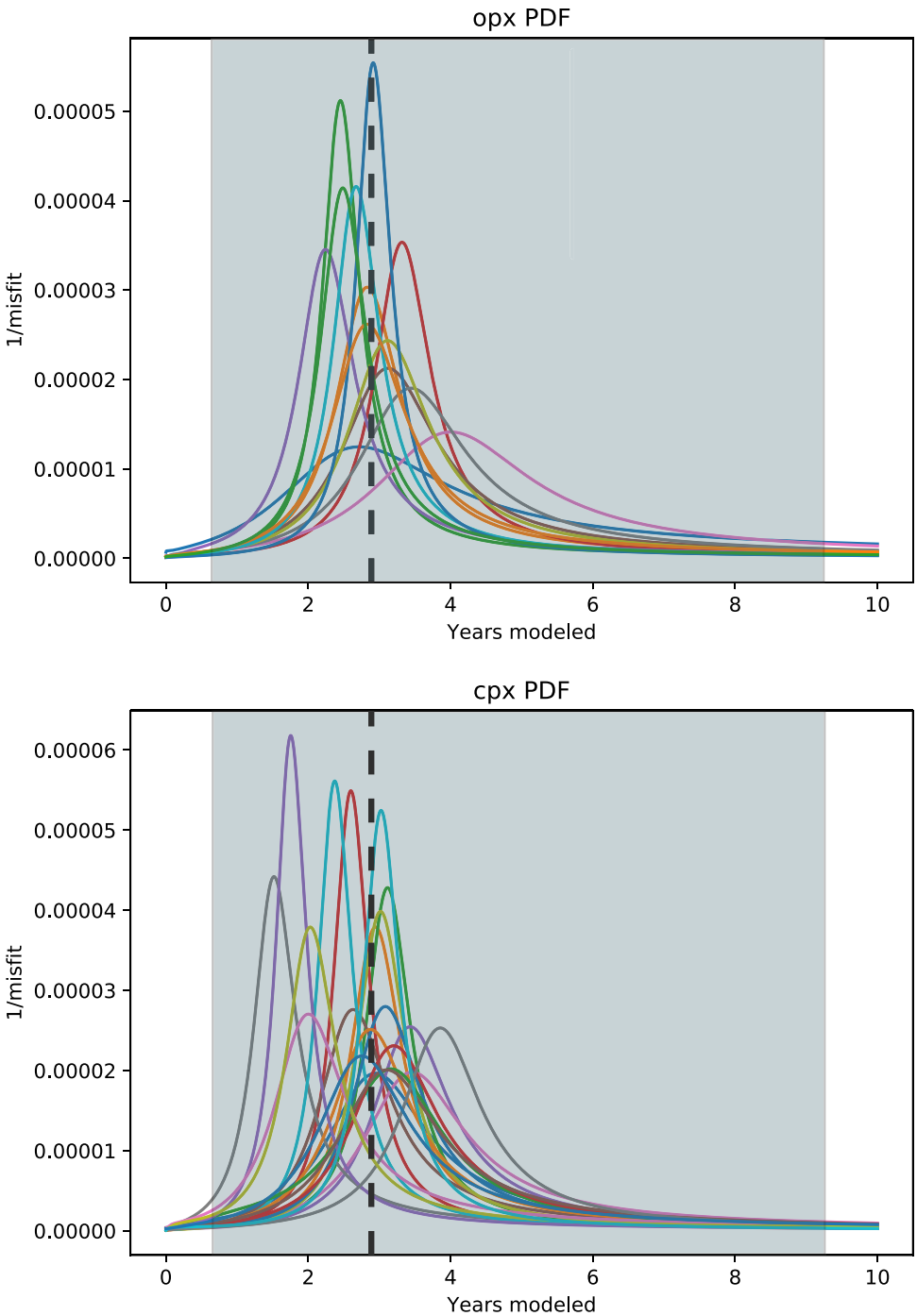

Fig. 11 Probability distribution functions of all opx and cpx diffusion modeling runs. The *y*-axis is the inverse value of the misfit determined during diffusion modeling; therefore, a higher value on the *y*-axis corresponds to lower misfit. The *x*-axis displays all times tested by the model, where the best fit time is indicated by a "peak" in misfit

Cooling and magma flux rates

The lack of amphibole found in the PMA and knowledge of the PMA phase diagram (Fig. 9) also provide constraints on the cooling history of the PMA. Because the PMA remained below the amphibole-in phase boundary during ascent, the cooling rate for the PMA is constrained to a maximum of ~ 5 °C/km, or a total of ~ 75 °C during the 15 km of ascent over several years. This is consistent with an eruption temperature of ~ 900 °C, which falls within the range of likely eruption temperatures for a hydrous primitive andesite. A minimum cooling rate would be dictated by an adiabatic ascent (~ 0.5 °C/km) or ~ 7.5 °C total over several years, putting the predicted eruption temperature at the high end of what is expected for a hydrous primitive andesite (~ 967.5 °C). Conductive cooling models predict cooling of ~ 100 °C in years to decades for 10–50 m thick dikes in country rock at ~ 450 °C (e.g., Rubin et al. 2017),

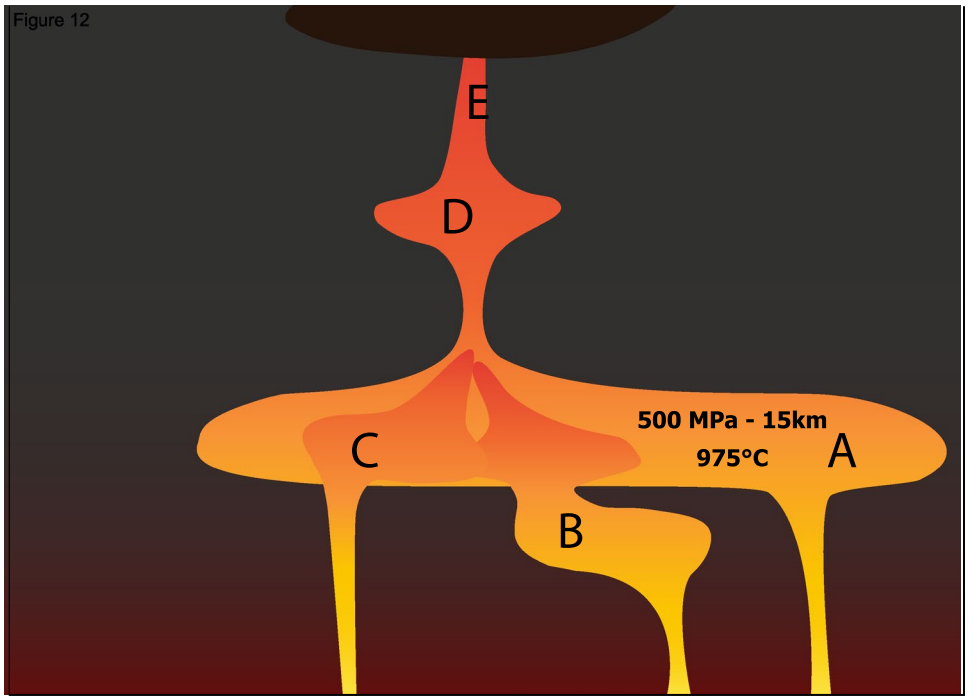

Fig. 12 Schematic figure of proposed mixing history. *A* source of Fe-rich cpx and opx cores. *B* source of slightly more primitive cores that show disequilibrium textures, likely due to mixing with more evolved magma *A*. *C* mafic recharge magma, source of Mg-rich rims on cpx and opx cores of *A* and *B*. *C* also introduces large, primitive olivine and opx phenocrysts that react with *A* and *B*, forming disequilibirum textures in some crystals. *D* subsequent crystalization of unzoned cpx pheocrysts due to cooling and fractionation. *E* skeletal olivine growth during final, rapid ascent and decompression

which is consistent with a cooling rate closer to the maximum predicted here for the PMA. Taken altogether, the PMA's characteristics suggests several hundredths of a cubic km of primitive hydrous magma fluxed through the upper crust over a period of several years, cooling 10's of degrees during transit.

Our access to this history may be a fortunate mistake due to the eruption of the PMA at a satellite vent to the main Mt. Shasta edifice that has remained exposed over the last ~ 700 ka. If representative, this fortunate mistake provides a window into the history of magma flux beneath the Mt. Shasta arc stratocone during the late Holocene. Christiansen et al. (2020) summarize Mt. Shasta as a ~ 400–450 km^3 composite edifice constructed by five main volcanic cones erupted from a cluster of central vents that grew intermittently over at least 700 ka. The compositional distribution is thought to be andesite > dacite > basalt (Hildreth 2007), which required ~ 1250 km^3 of primitive basalt to produce (Till et al. 2019). A simple back of the envelope calculation thus suggests ~ 2/3 of the volume of mantle primitive basalts fluxed into the base of crust were left behind in the crust at various stages of fractionation in this system. If we assume the erupted mafic magmas were fluxed through the crust in relatively small batches at rates analogous to the PMA's transit through the mid-to-upper crust, then the average Shasta hydrous mafic magma took years to decades to transit the 35–40 km thick crust in the region. The remaining majority of the edifice, the erupted andesitic and dacitic magmas, likely required longer crustal evolution + residence times, although maybe not significantly longer. U–Th–Ra isotope data on Shasta andesites and dacites suggests average crustal residence times of thousands to tens of thousands of years (Volpe 1992; Fabbrizio et al. 2009), although this may be affected by the extent of lower crustal melting and assimilation (Wende et al. 2015). Similarly, zircon geochronology on a granitoid block found within the Holocene Shastina lavas, the youngest Shasta cone building event, yield crystallization ages that overlap the radiocarbon ages for the Shastina deposits at 95% confidence, suggesting that the Shastina lavas may have been assembled within thousands of years. All the Shastina geochronology together indicates these lavas were erupted over a period of just 250 years (Christiansen et al. 2020). While this may be faster that some of the prior cone building events at Shasta, the data available suggests that that crustal magma flux and assembly occurred in discrete pulses that represent a minority of the 700 k.y. period during which the Mt. Shasta edifice was constructed. What dictated these short pulses of cone building at Mt. Shasta remains an outstanding question.

Diffusion modeling and volcanic monitoring

The growing popularity of using petrology to identify magmatic processes leading to eruption coupled with diffusion chronometry to determine the associated timescales points to a future with more robust conceptual and physical models of the run-up to volcanic eruptions and improved hazard mitigation and eruption forecasting. Recent work demonstrates the promise of an interdisciplinary approach that

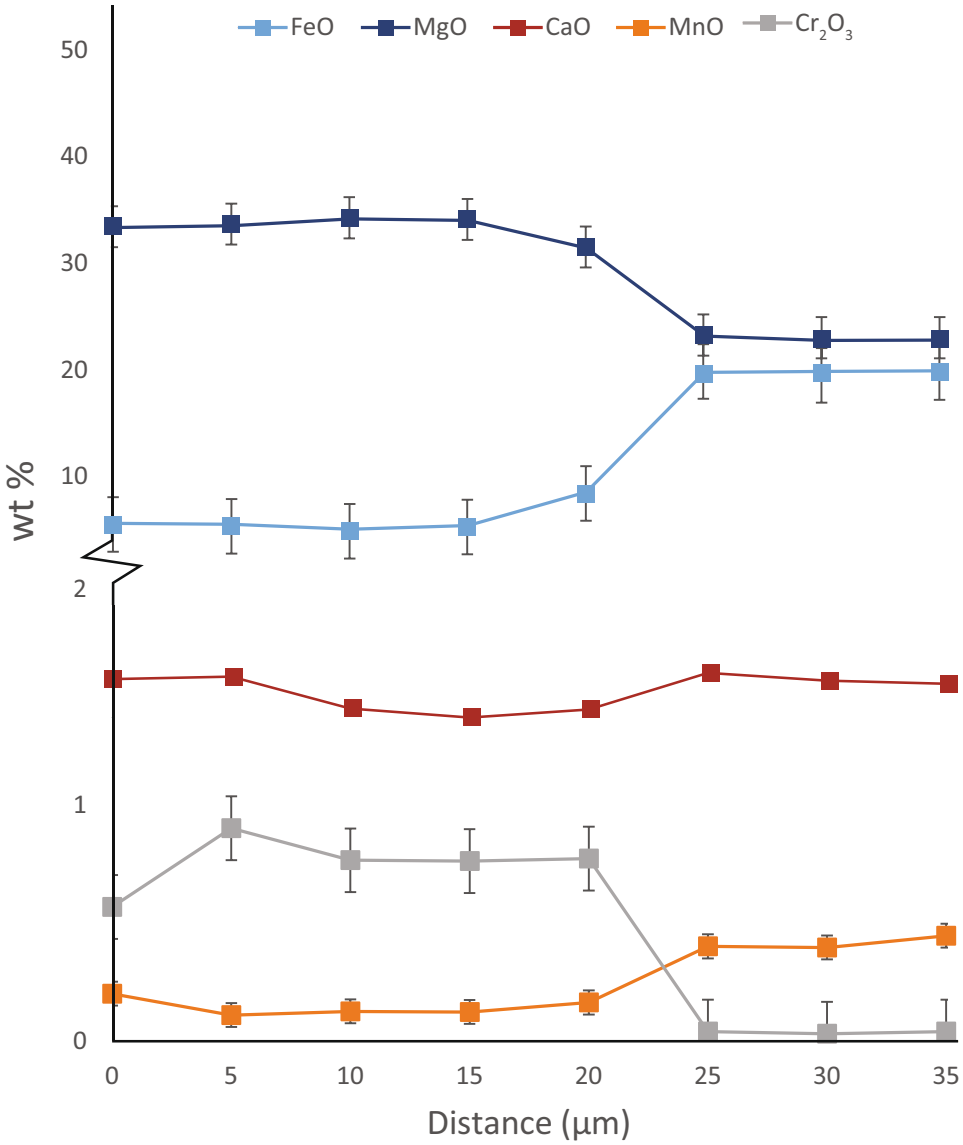

Fig. 13 Major element concentration profiles of representative, reversely zone orthopyroxene phenocryst with rim compositions of the left and core on the right. Error bars are standard error of the mean and sometimes smaller than the data point. The *y*-axis is split at 2 wt% to better resolve Cr, Ca, and Mn compositions. The primary elemental exchange is between Fe and Mg, though Mn sometimes substitutes for Mg. Cr displays a concentration change, but it is not over the full width of the diffusion profile (highlighted in green). Less evolved magmas tend to be enriched in Cr, suggesting the recharge magma was more primitive than the more evolved version it mixed with to form Mg-rich rims on pyroxene phenocrysts

Table 7 Summary of ascent rates from other studies

Method	Study	Ascent rate
Xenolith bearing magmas	Blatter and Carmichael (1998)	26,000 m/day
Olivine-hosted melt emabayments	Lloyd et al. (2014)	1.3 × 10^6 m/day
	Ferguson et al. (2016)	1.7 × 10^5–1.1 × 10^6 m/day
U-series isotopes	Mckenzie (2000)	27 m/day
Ni zonation in olivine	Ruprecht and Plank (2013)	68 m/day
	Mutch et al. (2019)	8000 m/day
Fe–Mg interdiffusion in cpx and opx	This study	5–30 m/day
	Hollyday et al. (2020)	2.5 m/day

couples magmatic timescales from diffusion chronometry to recorded seismicity data, where long-period seismicity can be temporally linked to magma recharge events. At Shishaldin volcano, timescales assessed via Fe–Mg interdiffusion in olivine showed magma mixing occurred ~ 50 days prior to eruption coinciding in time and space with early signals of unrest in the form of long period seismicity (Rassamussen et al. 2018). Similar relationships between magmatic processes at depth and long period seismicity have been shown in other volcanic systems including Mount St.

Helens (Saunders et al. 2012), Mt. Etna (Kahl et al. 2011, 2013; Cannata et al. 2018), Kilauea Iki (Rae et al. 2016), and Iceland (Pankurst et al. 2018). While volcano monitoring was not around ca. 700 ka leading up to the eruption of the PMA, today Mt. Shasta is instrumented with seismic and geodetic networks that the USGS and UNAVCO monitors daily, which have indicated a low level of activity for the last few decades. However, should future earthquake swarms indicative of magma movement in the middle to upper crust occur, the results presented herein provide the first estimates of the possible magma ascent rates and the time intervals that could accompany related magma ascent to eruption at Mt. Shasta.

Conclusions

Though originally thought to be a mantle-derived magma that rapidly ascended through the crust, our work reveals the Mt. Shasta primitive magnesian andesite while remarkably primitive also experienced a more complex history of crustal storage and mixing. Petrographic and geochemical analyses reveal a phenocryst assemblage with reverse chemical zoning representing mid-crustal mixing of batches of magma that represent various degrees of fractionation of a similar primary magma, with the last crustal mixing event occurring at approximately 500 MPa and 975 °C. Transit of the PMA from these conditions to eruption occurred over ~$2.9^{+6.5}_{-2.5}$ years at minimum average upper crustal ascent rate of 5 km/year (~2–38 km/year (~5–100 m/day) at 95% confidence), cooling the PMA a maximum of 75 °C before eruption**.** Along together, the PMA's characteristics suggests several hundredths of a cubic km of primitive hydrous magma fluxed through the upper crust over a period of several years, cooling 10's of degrees during transit. If this behavior is representative, ~the 10% mafic magmas erupted as part of the modern Shasta system, fluxed through the crust within decades. The remaining majority of the edifice, the erupted andesitic and dacitic magmas, required thousands to tens of thousands of years to flux through the crust and assemble, suggesting that crustal magma flux and assembly occurred in discrete pulses that represent a minority of the 700 k.y. period of Mt. Shasta edifice construction. What dictated the pulses of cone building at Mt. Shasta remains an outstanding question. Overall, the combined results of this study provide new estimates of the pre-eruptive history, ascent rates, and evolution of the Mt. Shasta primitive magnesian andesite, enriching our understanding primitive arc magma petrogenesis and informing volcanic hazard models for monogenetic, cinder cone eruptions in the Southern Cascades. Should future earthquake swarms indicative of magma movement in the middle to upper crust occur beneath Shasta, the results presented here provide the first estimates of the possible magma ascent rates and the time intervals that could accompany related magma ascent to eruption at Mt. Shasta.

Supplementary Information The online version contains supplementary material available at https://doi.org/10.1007/s00410-021-01853-x.

Acknowledgements This research was supported by an NSF CAREER Grant awarded to C. B. Till (EAR 1654584). Special thanks to T.L. Grove for mentorship in the field work, A. Wittman for assistance with the EPMA at ASU, the Washington State Geoanalytical Lab for geochemical analysis, and Spectrum Petrographics for thin section preparation. Samples for this study were collected from the Shasta-Trinity and Modoc National Forests, the ancestral tribal lands of the Shasta and Modoc peoples.

References

Allan AM, Mavko G (2013) The effect of adsorption and Knudsen diffusion on the steady-state permeability of microporous rocks. Geophysics 78(2):D75–D83

Baker MB, Grove TL, Price R (1994) Primitive basalts and andesites from the Mt. Shasta region, N. California: products of varying melt fraction and water content. Contrib Mineral Petrol 118(2):111–129

Barr J, Grove TL, Elkins-Tanton L (2007) High-magnesian andesite from Mount Shasta: a product of magma mixing and contamination, not a primitive melt: comment and reply: comment. Geology 35(1):e147–e147

Barth A, Newcombe M, Plank T, Gonnermann H, Hajimirza S, Soto GJ et al (2019) Magma decompression rate correlates with explosivity at basaltic volcanoes—constraints from water diffusion in olivine. J Volcanol Geothermal Res 387:106664

Blakely RJ, Jachens RC, Simpson RW, Couch RW (1985) Tectonic setting of the southern Cascade Range as interpreted from its magnetic and gravity fields. Geol Soc Am Bull 96(1):43–48

Blatter DL, Carmichael IS (1998) Hornblende peridotite xenoliths from central Mexico reveal the highly oxidized nature of subarc upper mantle. Geology 26(11):1035–1038

Cannata A, Di Grazia G, Giuffrida M, Gresta S, Palano M, Sciotto M et al (2018) Space-time evolution of magma storage and transfer at Mt. Etna Volcano (Italy): the 2015–2016 Reawakening of Voragine Crater. Geochem Geophys Geosyst 19(2):471–495

Cherniak DJ, Dimanov A (2010) Diffusion in pyroxene, mica and amphibole. Rev Mineral Geochem 72(1):641–690

Christiansen RL, Kleinhampl FJ, Blakely RJ, Tuchek ET, Johnson FL, Conyac MD (1977) Resource appraisal of the Mt. Shasta wilderness study area, Siskiyou County, California (No. USGS-OFR-77-250). Geological Survey, Menlo Park, CA (USA)

Christiansen RL, Calvert AT, Champion DE, Gardner CA, Fierstein JE, Vazquez JA (2020) The remarkable volcanism of Shastina, a stratocone segment of Mount Shasta, California. Geosphere 16(5):1153–1178

Conway CE, Chamberlain KJ, Harigane Y, Morgan DJ, Wilson CJN (2020) Rapid assembly of high-Mg andesites and dacites by magma mixing at a continental arc stratovolcano. Geology 48(10):1033–1037

Costa F, Morgan D (2011) Time constraints from chemical equilibration in magmatic crystals. Timescales of magmatic processes: from core to atmosphere. Wiley, Chichester, pp 125–159

Costa F, Shea T, Ubide T (2020) Diffusion chronometry and the timescales of magmatic processes. Nat Rev Earth Environ 1(4):201–214

DeMets C, Gordon RG, Argus DF (2010) Geologically current plate motions. Geophys J Int 181(1):1–80
Dohmen R, Ter Heege JH, Becker HW, Chakraborty S (2016) Fe-Mg interdiffusion in orthopyroxene. Am Miner 101(10):2210–2221
Embley RW, Wilson DS (1992) Morphology of the Blanco transform fault zone-NE Pacific: implications for its tectonic evolution. Mar Geophys Res 14(1):25–45
Ewert JW, Diefenbach AK, Ramsey DW (2018) 2018 update to the US Geological Survey national volcanic threat assessment (No. 2018-5140). US Geological Survey
Fabbrizio A, Schmidt MW, Günther D, Eikenberg J (2009) Experimental determination of Ra mineral/melt partitioning for feldspars and 226Ra-disequilibrium crystallization ages of plagioclase and alkali-feldspar. Earth Planet Sci Lett 280(1–4):137–148
Ferguson DJ, Gonnermann HM, Ruprecht P, Plank T, Hauri EH, Houghton BF, Swanson DA (2016) Magma decompression rates during explosive eruptions of Kīlauea volcano, Hawaii, recorded by melt embayments. Bull Volcanol 78(10):71
Fuis GS, Zucca JJ, Mooney WD, Milkereit B (1987) A geologic interpretation of seismic-refraction results in northeastern California. Geol Soc Am Bull 98(1):53–65
Gill JB (1981) Orogenic andesites and plate tectonics. Springer, New York
Green NL, Harry DL (1999) On the relationship between subducted slab age and arc basalt petrogenesis, Cascadia subduction system, North America. Earth Planet Sci Lett 171(3):367–381
Griscom A (1980) Cascade range and Modoc plateau. Bull Calif Div Mines Geol 205:36–38
Grove T, Parman S, Bowring S, Price R, Baker M (2002) The role of an H 2 O- rich fluid component in the generation of primitive basaltic andesites and andesites from the Mt. Shasta region, N California. Contrib Mineral Petrol 142(4):375–396
Grove TL, Elkins-Tanton LT, Parman SW, Chatterjee N, Müntener O, Gaetani GA (2003) Fractional crystallization and mantle-melting controls on calc-alkaline differentiation trends. Contrib Miner Petrol 145(5):515–533
Grove TL, Baker MB, Price RC, Parman SW, Elkins-Tanton LT, Chatterjee N, Müntener O (2005) Magnesian andesite and dacite lavas from Mt. Shasta, northern California: products of fractional crystallization of H 2 O-rich mantle melts. Contrib Mineral Petrol 148(5):542–565
Grove TL, Till CB, Krawczynski MJ (2012) The role of H2O in subduction zone magmatism. Ann Rev Earth Planet Sci 40:413–439. https://doi.org/10.1146/annurev-earth-042711-105310
Hawkesworth C, George R, Turner S, Zellmer G (2004) Time scales of magmatic processes. Earth Planet Sci Lett 218(1–2):1–16
Hildreth W (2007) Quaternary magmatism in the Cascades—geologic perspectives. Professional Papers of the United States Geological Survey, 1744.
Hollyday AE, Leiter SH, Walowski KJ (2020) Pre-eruptive storage, evolution, and ascent timescales of a high-Mg basaltic andesite in the southern Cascade Arc. Contrib Miner Petrol 175(9):1–21
Kahl M, Chakraborty S, Costa F, Pompilio M (2011) Dynamic plumbing system beneath volcanoes revealed by kinetic modeling, and the connection to monitoring data: an example from Mt. Etna. Earth Planet Sci Lett 308(1–2):11–22
Kahl M, Chakraborty S, Costa F, Pompilio M, Liuzzo M, Viccaro M (2013) Compositionally zoned crystals and real-time degassing data reveal changes in magma transfer dynamics during the 2006 summit eruptive episodes of Mt. Etna. Bull Volcanol 75(2):692
Kelemen PB, Yogodzinski G (2007) High-magnesian andesite from Mount Shasta: a product of magma mixing and contamination, not a primitive melt: comment and reply: comment. Geology 35(1):e149–e150
Kelemen PB, Hanghøj K, Greene AR (2013) One view of the geochemistry of subduction-related magmatic arcs, with an emphasis on primitive andesite and lower crust. Treatise Geochem 3:659
Krawczynski MJ, Grove TL, Behrens H (2012) Amphibole stability in primitive arc magmas: effects of temperature, H 2 O content, and oxygen fugacity. Contrib Miner Petrol 164(2):317–339
Krimer D, Costa F (2017) Evaluation of the effects of 3D diffusion, crystal geometry, and initial conditions on retrieved time-scales from Fe–Mg zoning in natural oriented orthopyroxene crystals. Geochim Cosmochim Acta 196:271–288
Le Voyer M, Rose-Koga EF, Shimizu N, Grove TL, Schiano P (2010) Two contrasting H_2O-rich components in primary melt inclusions from Mount Shasta. J Petrol 51(7):1571–1595
Lloyd AS, Ruprecht P, Hauri EH, Rose W, Gonnermann HM, Plank T (2014) NanoSIMS results from olivine-hosted melt embayments: magma ascent rate during explosive basaltic eruptions. J Volcanol Geoth Res 283:1–18
Mangan M, Ball J, Wood N, Jones JL, Peters J, Abdollahian N et al (2019) California's exposure to volcanic hazards (No. 2018-5159). US Geological Survey
McKenzie D (2000) Constraints on melt generation and transport from U-series activity ratios. Chem Geol 162(2):81–94
Müller T, Dohmen R, Becker HW, Ter Heege JH, Chakraborty S (2013) Fe–Mg interdiffusion rates in clinopyroxene: experimental data and implications for Fe–Mg exchange geothermometers. Contrib Miner Petrol 166(6):1563–1576
Mutch EJ, Maclennan J, Shorttle O, Edmonds M, Rudge JF (2019) Rapid transcrustal magma movement under Iceland. Nat Geosci 12(7):569–574
Myers ML, Wallace PJ, Wilson CJN, Watkins JM, Liu Y (2018) Ascent rates of rhyolitic magma at the onset of three caldera-forming eruptions. Am Mineral 103:952–965. https://doi.org/10.2138/am-2018-6225
Myers ML, Wallace PJ, Wilson CJN (2019) Inferring magma ascent timescales and reconstructing conduit processes in explosive rhyolitic eruptions using diffusive losses of hydrogen from melt inclusions. J Volcanol Geothermal Res 369:95–112. https://doi.org/10.1016/j.jvolgeores.2018.11.009
Pankhurst MJ, Morgan DJ, Thordarson T, Loughlin SC (2018) Magmatic crystal records in time, space, and process, causatively linked with volcanic unrest. Earth Planet Sci Lett 493:231–241
Petrone CM, Bugatti G, Braschi E, Tommasini S (2016) Pre-eruptive magmatic processes re-timed using a non-isothermal approach to magma chamber dynamics. Nat Commun 7:12946
Pioli L, Azzopardi BJ, Cashman KV (2009) Controls on the explosivity of scoria cone eruptions: magma segregation at conduit junctions. J Volcanol Geoth Res 186(3–4):407–415
Putirka KD (2008) Thermometers and barometers for volcanic systems. Rev Mineral Geochem 69(1):61–120
Quick JE (1981) Petrology and petrogenesis of the Trinity peridotite, an upper mantle diapir in the eastern Klamath Mountains, northern California. J Geophys Res Solid Earth 86(B12):11837–11863
Rae AS, Edmonds M, Maclennan J, Morgan D, Houghton B, Hartley ME, Sides I (2016) Time scales of magma transport and mixing at Kīlauea Volcano Hawai'i. Geology 44(6):463–466
Rasmussen DJ, Plank TA, Roman DC, Power JA, Bodnar RJ, Hauri EH (2018) When does eruption run-up begin? Multidisciplinary insight from the 1999 eruption of Shishaldin volcano. Earth Planet Sci Lett 486:1–14
Rubin AE, Cooper KM, Till CB, Kent AJ, Costa F, Bose M et al (2017) Rapid cooling and cold storage in a silicic magma reservoir recorded in individual crystals. Science 356(6343):1154–1156
Ruprecht P, Plank T (2013) Feeding andesitic eruptions with a high-speed connection from the mantle. Nature 500(7460):68
Ruscitto DM, Wallace PJ, Johnson ER, Kent AJR, Bindeman IN (2010) Volatile contents of mafic magmas from cinder cones in

the Central Oregon High Cascades: Implications for magma formation and mantle conditions in a hot arc. Earth Planet Sci Lett 298(1–2):153–161

Ruscitto DM, Wallace PJ, Kent AJR (2011) Revisiting the compositions and volatile contents of olivine-hosted melt inclusions from the Mount Shasta region: implications for the formation of high-Mg andesites. Contrib Mineral Petrol 162(1):109–132

Saunders K, Blundy J, Dohmen R, Cashman K (2012) Linking petrology and seismology at an active volcano. Science 336(6084):1023–1027

Sisson TW, Layne GD (1993) H2O in basalt and basaltic andesite glass inclusions from four subduction-related volcanoes. Earth Planet Sci Lett 117:619–635. https://doi.org/10.1016/0012-821X(93)90107-K

Shamloo HI, Till CB (2019) Decadal transition from quiescence to supereruption: petrologic investigation of the Lava Creek Tuff, Yellowstone Caldera, WY. Contrib Mineral Petrol 174(4):1–18

Streck MJ, Leeman WP (2018) Petrology of "Mt. Shasta" high-magnesian andesite (HMA): a product of multi-stage crustal assembly. Am Mineral J Earth Planet Mater 103(2):216–240

Streck MJ, Leeman WP, Chesley JT (2007) High-magnesian andesite from Mount Shasta: A product of magma mixing and contamination, not a primitive melt: comment and reply: reply. Geology 35(1):e148–e148

Syracuse EM, van Keken PE, Abers GA (2010) The global range of subduction zone thermal models. Phys Earth Planet Inter 183(1–2):73–90

Till CB, Grove TL, Carlson RW, Donnelly-Nolan JM, Fouch MJ, Wagner LS, Hart WK (2013) Depths and temperatures of <10.5 Ma mantle melting and the lithosphere-asthenosphere boundary below southern Oregon and northern California. Geochem Geophys Geosyst 14:864–879. https://doi.org/10.1002/ggge.20070

Till CB, Vazquez JA, Boyce JW (2015) Months between rejuvenation and volcanic eruption at Yellowstone caldera, Wyoming. Geology 43(8):695–698

Till CB, Kent AJR, Abers GA, Janiszewski HA, Gaherty JB, Pitcher BW (2019) The causes of spatiotemporal variations in erupted fluxes and compositions along a volcanic arc. Nat Commun 10:1–12

van Keken PE, Hacker BR, Syracuse EM, Abers GA (2011) Subduction factory: 4. Depth-dependent flux of H_2O from subducting slabs worldwide. J Geophys Res Solid Earth 116:B01401. https://doi.org/10.1029/2010JB007922

Volpe AM (1992) ^{238}U-^{230}Th-^{226}Ra disequilibirium in young Mt. Shasta andesites and dacites. J Volcanol Geoth Res 53(1–4):227–238

Walowski KJ, Wallace PJ, Hauri EH, Wada I, Clynne MA (2015) Slab melting beneath the Cascade Arc driven by dehydration of altered oceanic peridotite. Nat Geosci 8:404–408. https://doi.org/10.1038/ngeo2417

Wende AM, Johnson CM, Beard BL (2015) Tracing changes in mantle and crustal influences in individual cone-building stages at Mt. Shasta using U-Th and Sr isotopes. Earth Planet Sci Lett 428(C):11–21